Submitted to ApJ

SMARTS Optical and infrared monitoring of 12 gamma-ray bright blazars

E. W. Bonning[1], C. M. Urry[1] C. Bailyn[2], M. Buxton[2], R. Chatterjee[2], P. Coppi[2], G. Fossati[4], J. Isler[1], L. Maraschi[3]

ABSTRACT

We present multiwavelength data for twelve blazars observed from 2008-2010 as part of an ongoing optical-infrared photometric monitoring project. Sources were selected to be bright, southern blazars observed by the *Fermi* Gamma-Ray Space Telescope, with daily and weekly gamma-ray fluxes made available from the start of the *Fermi* mission. Light curves are presented for the twelve blazars in BVRJK (0.4 to 2.2 μm) at near-daily cadence. We find that optical and infrared fluxes are well correlated in all sources, with no lag between bands. Gamma-ray bright flat spectrum radio quasars (FSRQs) in our sample have optical/infrared emission correlated with gamma-rays with lags of less than one day, consistent with inverse Compton-scattering leptonic models for GeV emission. In FSRQs, the variability amplitude decreases towards shorter wavelengths, consistent with the presence of a thermal emission component from the accretion disk varying on significantly longer timescales than the jet synchrotron emission. In BL Lac objects, variability is mainly constant across wavelengths, consistent with a weak or radiatively inefficient disk. Also consistent with this picture, FSRQs have redder optical-infrared colors when they are brighter, while BL Lac objects show no such trend. Several objects show complicated color-magnitude behavior: AO 0235+164 appears in two different states depending on whether it is gamma-ray bright or not. OJ 287 and 3C 279 show some hysteresis

[1]Department of Physics and Yale Center for Astronomy and Astrophysics, Yale University, PO Box 208121, New Haven, CT 06520-8120; erin.bonning@yale.edu

[2]Department of Astronomy and Yale Center for Astronomy and Astrophysics, Yale University, PO Box 208101, New Haven, CT 06520-8101

[3]INAF - Osservatorio Astronomico di Brera, V. Brera 28, I-20100 Milano, Italy

[4]Department of Physics and Astronomy, Rice University, Houston, TX 77005

tracks in their color-magnitude diagrams. Individual flares may be achromatic or otherwise depart from the trend, suggesting different jet components becoming important at different times. We present a time-dependent spectral energy distribution of the bright FSRQ 3C 454 during December 2009 flare, which is well fit by an external Compton model in the bright state, although day to day changes in the course of the flare pose challenges to a simple one-zone model. All data from the SMARTS monitoring program are publicly available on our website.

Subject headings: galaxies: active — quasars: general — black hole physics — BL Lacertae objects

1. Introduction

Blazars form a sub-class of active galactic nuclei (AGN) with a bright, relativistic jet viewed closely along our line of sight (Urry & Padovani 1995). Blazars are often very luminous and violently variable over a large range of wave bands from radio to gamma-rays. Spectral energy distributions (SEDs) of blazars are characterized by two broad components: one at the infrared-optical/UV frequencies and the other at hard X-ray-gamma-ray energies. The radio to optical/UV emission in blazars is interpreted as synchrotron radiation by the energetic electrons in the jet (Konigl 1981; Urry & Mushotzky 1982) while the mechanism of the high energy emission (i.e., X-rays and gamma-rays) is less certain. It may be due to the inverse-Compton scattering of seed photons by the same relativistic electrons responsible for the synchrotron radiation (the so-called leptonic models; e.g. Böttcher 2007) or due to synchrotron radiation of protons co-accelerated with the electrons in the jet, interactions of these highly relativistic protons with external radiation fields, or proton-induced particle cascades (hadronic models; e.g. Mücke & Protheroe 2001; Mücke et al. 2003).

Both leptonic and hadronic models can successfully explain the SEDs observed so far, but they have very different implications for the kinetic power of the jet and hence how it is produced and its influence on its environment. In the case of leptonic models, the low-energy seed photons may be the synchrotron photons produced within the jet (synchrotron self-Compton, or SSC; Jones et al. 1974) or thermal emission from outside the jet. External Compton (EC) scenarios produce high energy emission from upscattering photons from the accretion disk, broad line region (BLR), or dusty torus (Sikora et al. 1994; Dermer & Schlickeiser 1993; Ghisellini & Madau 1996; Tavecchio et al. 2000; Ghisellini & Celotti 2001). The jet plasma may consist of electrons and protons, electrons and positrons, or a combination of the two (Ghisellini & Tavecchio 2010; Sikora & Madejski 2000).

Knowing the composition of the jet is necessary to deduce its kinetic power, which in turn reflects how it is launched, accelerated, and collimated. Studying the SED and its variation with time allows us to determine the radiation mechanism, and thus the physical parameters of the emission region, such as the magnetic field, particle number density, and bulk velocity of the plasma.

Until recently, blazar SED studies occurred primarily when the brightness of a blazar significantly increased in one or multiple wave bands. Due to the difficulty of coordinating large multiwavelength campaigns, data in other wavebands were often non-simultaneous. The near-continuous monitoring activity of the Large Area Telescope (LAT) instrument on board the *Fermi Gamma-Ray Space Telescope*, launched in 2008, provides the opportunity to study the variable SEDs of a large sample of blazars with truly simultaneous multi-frequency data. Although many blazars radiate most of their energy in the gamma-ray band, it is the characterization of both broad components of the blazar SEDs and their relative variation with time that allows us to infer the physics of these sources. Specifically, correlations between variations in gamma-ray flux and those at lower energies are useful indicators of the relative locations of emission regions and the radiation mechanism(s).

Fermi/LAT provides regular and well sampled gamma-ray light curves of a large sample of blazars. Obtaining the same quality data at optical and infrared wavelengths is equally important. We use the meter-class telescopes of the Small and Moderate Aperture Research Telescope System (SMARTS) to carry out photometric monitoring of bright southern gamma-ray blazars on a regular cadence, at both optical and near-infrared wavelengths.

In this paper, we report on the Yale/SMARTS program in 2008-2010 to carry out photometric monitoring of all bright southern Fermi-LAT monitored blazars on a regular cadence, at both optical and near-infrared wavelengths. We present light curves for the blazars with the greatest coverage, and refer the reader to our website[5] for the full data set. In addition, we report on gamma-ray/optical-IR cross-correlation functions for several blazars and show an example of how a variable SED has the potential to constrain the physics of a jet and/or accretion disk. Finally, we discuss the color-magnitude diagrams for blazars and how these can yield broad inferences about particle acceleration and radiative losses in blazar jets.

In § 2 we present the sample selection and data reduction and present the multi-wavelength light curves .In § 3, we discuss the variability characteristics of the blazars in our sample, including cross-correlations between gamma-ray and optical-IR variations, frequency-dependent variability amplitude, and color-magnitude relations for our sample of

[5]http://www.astro.yale.edu/smarts/fermi

blazars. We discuss SED fits for a sample blazar flare in § 5. In § 6 we present the summary and conclusions.

2. Sample Selection and Data Analysis

The SMARTS blazar sample was initially (in 2008) defined to include all LAT-monitored blazars on the initial public release list with declination $< 20°$. Prior to the launch of Fermi, the list of sources which were to have fluxes made publicly available consisted mainly of bright blazars observed by EGRET. Additional sources were added to our monitoring campaign as they were added to the public LAT source list or were the target of a multi-wavelength campaign. We observed these twelve sources with a cadence of approximately once every three days. Brighter or flaring sources were observed nightly. The SMARTS source list, including positions, redshifts, and observation timeframe is given in Table 1. Each of the blazars is identified by its spectral class: flat-spectrum radio quasar (FSRQ), low frequency-peaked BL Lac object (LBL), or high frequency-peaked BL Lac (HBL). These form a rough sequence of decreasing continuum luminosity and emission line luminosity (Fossati et al. 1998). The most luminous blazars (FSRQ and LBL) have their synchrotron peak at IR/optical wavelengths and the inverse Compton peak in GeV gamma-rays so they form the bulk of our monitored sample.

The 12 blazars were observed with the SMARTS 1.3m telescope and ANDICAM instrument (DePoy et al. 2003). ANDICAM is a dual-channel imager with a dichroic that feeds an optical CCD and an IR imager, which can obtain simultaneous data from 0.4 to 2.2 μm. Observations were taken in B, V, R, J, and K bands, except for two sources: PKS 0528 and 3C 273 for which K-band images were not obtained. The former was below the K-band detection limit; the latter, being very bright, had very short exposure times in optical bands.Since IR images are taken simultaneously with optical, there was only sufficient time for J-band images to be obtained for 3C 273. Additionally, spectra were obtained for a number of the brighter sources, using the SMARTS RCSPEC+1.5-meter telescope. These data will be discussed in forthcoming paper (Isler et al. *in prep*).

Optical data were bias-subtracted, overscan-subtracted, and flat fielded using the CCDPROC task in IRAF. Infrared data were sky-subtracted, flat fielded, and dithered images combined using in-house IRAF scripts. Slight blemishes reflecting the dither pattern are apparent in the final images,but introduce at most a 0.1% photometric error.

Optical and infrared aperture photometry was performed using the PHOT task in IRAF. The raw photometry of comparison stars in the field of the blazar was calibrated using

photometric zeropoints that were measured from ANDICAM observations during 2008-2009 of optical (Landolt 1992) and near-infrared (Persson et al. 1998) primary standards for each filter, correcting for atmospheric extinction derived from all the standards taken together. The number of photometric nights available for the calibration for each field and each filter differs, but ranges from 40-128 nights in the optical, and 13-98 nights for the near-infrared. The average of the comparison stars were used as a basis of differential photometry with respect to the blazar for all observations.

The optical and IR light curves for the monitored blazars through July 2010 are shown in Figure 1. (At the time of writing, some third-year SMARTS data are already available online but the basic scientific results do not change for the 12 blazars discussed here.) These figures include daily and weekly gamma-ray fluxes from the *Fermi*/LAT public light curves for those sources bright enough in the gamma-ray that these are measureable. The optical and infrared light curves and calibrated magnitudes are available online at the Yale SMARTS Blazar site[5]. Optical and infrared finding charts are shown in Appendix A and B. Calibrated magnitudes for the comparison stars in each blazar field are given in Appendix C.

The error in calibrating the secondary star magnitudes was found by calculating the 1-σ standard error of the mean over the number of photometric nights mentioned above. Results that were greater than $\pm$ 3σ from the mean were rejected and the mean and σ were recalculated. This procedure was repeated until no more rejections were made. The resulting errors are given in Tables C.1. and C.2. These errors do not account for systematic errors associated with effects such as the difference in effective filter responses between SMARTS and the standard system. Such systematics are likely to contribute a few hundredths of a magnitude of calibration error.

Previous work with SMARTS photometry (Buxton et al. 2011, *submitted*) has led to an understanding of the errors in differential photometry for point sources as a function of count rate. Based on this work, we find errors as low as 0.01 magnitudes in the optical and 0.02 magnitudes in the IR for bright sources (<16 mag in the optical and <13 mag in IR), and up to ten times that for sources near the detection limit, which varies depending on the exposure time. We note that these errors are random errors in the individual points, rather than systematic offsets in the magnitude system, as is the case for the calibration errors.

---

[5]http://ned.ipac.caltech.edu/ The NASA/IPAC Extragalactic Database (NED) is operated by the Jet Propulsion Laboratory, California Institute of Technology, under contract with the National Aeronautics and Space Administration.

Name	R.A. & Dec. (J2000) [h:m:s] [d:m:s]	Class	z	Dates (MJD)
PKS 0208−512	02:10:46.2 −51:01:01	FSRQ	1.003	54640 – 55282
AO 0235+16	02:38:38.9 +16:36:59	LBL	0.940	54662 – 55487
PKS 0528+134	05:30:56.4 +13:31:55	FSRQ	2.060	54701 – 55511
OJ 287	08:54:48.8 +20:06:31	LBL	0.306	54777 – 55500
3C 273	12:29:06.7 +02:03:09	FSRQ	0.158	54603 – 55412
3C 279	12:56:11.1 −05:47:21	FSRQ	0.536	54603 – 55416
PKS 1406−076	14:08:56.5 −07:52:27	FSRQ	1.494	54501 – 55385
PKS 1510−08	15:12:50.5 −09:06:00	FSRQ	0.360	54603 – 55464
PKS 1622−29	16:26:06.0 −29:51:27	FSRQ	0.815	54501 – 55481
PKS 1730−130	17:33:02.6 −13:04:49	FSRQ	0.902	54603 – 55494
PKS 2155−304	21:58:52.0 −30:13:32	HBL	0.112	54603 – 55557
3C 454.3	22:53:57.7 +16:08:54	FSRQ	0.859	54640 – 55545

Table 1: The SMARTS blazar sample. Coordinates and redshifts from NED. Dates indicate limits of R-band observations reported here. Other bands may have slightly different date ranges. Full data are available online.

3. Results and Discussion

3.1. Multiwavelength Cross-Correlation Results

Every blazar in our sample is highly variable in gamma-rays and, in most cases, in the optical/IR as well; only 3C273 shows minimal variations in the optical/IR. The optical, near-infrared and gamma-ray light curves are shown in Figure 1.

Strong variations at optical and near-infrared wavelengths are well correlated, with no lag. Note that given our daily cadence, we are sensitive only to lags longer than a couple of days. Figure 2 shows two examples of the excellent correlation between optical (B-band) and IR (J-band) for two blazars: PKS 2155-304 (an HBL, Fig. 2a), and 3C 279 (an FSRQ, Fig. 2b). The other 10 blazars show similar strong correlation, although for fainter sources the errors are much larger. For all 12 blazars, cross correlations of the optical with the near IR are consistent with zero lag.

Six blazars — four FSRQs, one LBL, and one HBL — were bright enough during 2008–2010 to be regularly detected by Fermi LAT in one-day time bins. In three cases, the optical-IR variability is reasonably well-correlated with the gamma rays: 3C454.3 (Bonning et al. 2009), PKS 1510-089 (Marscher et al. 2010), and AO 0235+164 (Agudo et al. 2011)

(the gamma-ray - infrared discrete correlation function for the latter is shown in Fig. 3). The FSRQs 3C 273 and 3C 279, and the HBL PKS 2155-304, do not show such significant correlations. The strongly disk-dominated FSRQ 3C 273, shows little to no variability in the optical/IR bands (fluctuations on the order of 1%) compared to the variations by a factor of several to 10 in gamma-rays. The small fractional variation at optical/IR frequencies in 3C 273 may be due to the relatively large luminosity of the accretion disk (Ramos et al. 1997), since the disk probably does not vary in the optical/IR over time scales as short as the gamma rays. For 3C 279, optical/IR-gamma ray correlations have been reported by Abdo et al. (2010) who note the coincidence of a gamma-ray flare with a strong change in optical polarization angle. However, our SMARTS data show larger amplitude changes (by several orders of magnitude) than the gamma-ray data, over both the first and second years of *Fermi* observations. The one HBL with high enough gamma-ray flux to appear consistently in the LAT daily fluxes, PKS 2155-304, shows variations of a factor of 2-3 in gamma-rays, along with longer-timescale variations in the optical-IR, but the two appear to be uncorrelated.

The close correlation of optical/IR and gamma-ray fluxes strongly favors leptonic models over hadronic models. In the latter, the two broad components of the SED should vary almost independently, while in leptonic models, the two peaks are should vary together. In the FSRQs, the peak of the low energy component of the SED is in the far-IR, longward of the SMARTS bands, while the high-energy component peaks in or near the Fermi LAT energy range. In terms of simple homogeneous leptonic models, the SMARTS data generally sample emission from higher energy electrons than the Fermi LAT data. (can obviously change if the SED peak moves, as in a major acceleration event, e.g. Pian et al. 1998, for the case of Mrk 501). More realistic electron distributions and/or geometries will complicate this picture, but in any case, there are multiple plausible reasons for variations in the strength of the optical-IR versus gamma-ray correlations among the FSRQs in our sample.

3.2. Excess Variance

Most blazars are strongly variable at gamma-ray energies and in the optical/IR. To quantify and compare the degree of variability in different blazars, and in different bands for the same blazar, we calculate the "excess variance," which is the fractional root-mean-squared variability amplitude normalized by the mean flux:

$$F_{\rm var} = \sqrt{\frac{{\rm S}^2 - \overline{\sigma_{\rm err}^2}}{\overline{x}^2}} \quad , \tag{1}$$

where S is the variance, $\sigma_{\rm err}$ is the observational uncertainty, and $\overline{x}$ is the mean of the data (Nandra et al. 1997; Edelson et al. 2002; Vaughan et al. 2003). The values of $F_{\rm var}$ calculated

for SMARTS and Fermi LAT data are listed in Table 2. In cases where K-band observations did not cover the same time periods as the other filters, we omit the K-band values.

The IR/optical/UV emission from blazars is a combination of thermal emission from a (possibly weak) accretion disk and relativistically beamed nonthermal emission from a jet. The disk emission peaks in the UV band so its relative contribution in optical/IR bands decreases toward longer wavelengths. Since the disk emission comes from $\gtrsim 10^4$ r_g (Malkan 1983; Sun & Malkan 1989), it is almost certainly less rapidly variable than from the jet. Therefore, on the timescales considered here, we expect the variability amplitude in the optical/IR to increase with wavelength, i.e., infrared bands to vary more than the optical. This is precisely the effect seen in Table 2 for the FSRQ: the overall variability amplitude decreases toward the B-band. In contrast, this trend is not seen for the LBLs AO 0235+164 and OJ 287, or the HBL PKS 2155-304. This is consistent with the fact that FSRQs have strong emission lines, implying a radiatively efficient accretion disk, and BL Lac objects, having weak emission lines, are likely to have weakly accreting or radiatively inefficient disks.

Name	Class	K	J	R	V	B	γ
PKS 0208-512	FSRQ	0.48	0.52	0.49	0.45	0.46	–
AO 0235+16	LBL	1.22	1.46	1.44	1.43	1.39	0.38
PKS 0528+134	FSRQ	–	0.70	0.30	0.25	0.34	–
OJ 287	LBL	0.45	0.37	0.42	0.44	0.45	–
3C 273	FSRQ	–	0.13	0.041	0.044	0.042	0.77
3C 279	FSRQ	0.96	0.80	0.84	0.89	0.87	0.38
PKS 1406-076	FSRQ	–	0.61	0.49	0.49	0.42	–
PKS 1510−08	FSRQ	–	1.04	0.94	0.93	0.81	0.56
PKS 1622-29	FSRQ	0.68	0.54	0.41	0.33	0.28	–
PKS 1730-130	FSRQ	0.59	0.48	0.39	0.34	0.36	–
PKS 2155-304	HBL	0.37	0.36	0.35	0.35	0.35	0.25
3C 454.3	FSRQ	0.81	0.77	0.68	0.62	0.59	1.40

Table 2: Fractional variability amplitude (as defined in Eqn.(1) for observed IR, optical, and gamma-rays. The gamma-ray values are listed only for blazars bright enough to be detected in daily *Fermi*/LAT averages.

4. Color-magnitude variations

We present in Figure 4 the relation between IR (J-band) magnitude and optical-IR spectral shape of the low-energy peak of the SED (given by $B - J$ color, such a *larger* value corresponds to a *redder* color). Overall, luminous blazars (FSRQs) are redder when brighter and bluer when fainter. A typical example is shown in Fig. 4i (PKS 1622-29). As the source varies in brightness, the color changes along a narrow locus in the color-magnitude plane, such that when the source is brighter, the color gets redder. Conversely, when the source is fainter, the color gets bluer (although the SED remains synchrotron-dominated and therefore red). This 'flattening' of the SED in faint states suggests a strong, blue accretion disk component is mixed with redder jet emission, which may only be visible as a typical 'blue bump' in extremely faint states (Raiteri et al. 2007, e.g. as observed in 3C 454.3 by). Most of our FSRQs (with exceptions noted below) follow this redder-when-brighter track, consistent with FSRQs having luminous accretion disks as evidenced by their typically strong emission lines.

Although the FSRQs mostly show redder-when-brighter trends, they can also show more complicated behavior. For example, the May 2010 flare in PKS 1510-089 (indicated by arrows in Fig. 4h) was essentially achromatic and, unlike its other flares, had a much larger amplitude than the associated gamma-ray flare (c.f. Fig. 1h). Such anomalous flares indicate the interplay of distinct components in the source; in the case of PKS 1510-089, the sharp achromatic flare could be caused by a plasma blob hitting a transverse shock in the jet (Marscher et al. 2010). (More speculatively, achromatic flares could be caused by gravitational microlensing in the halo of our galaxy, as in the MACHO experiment (Alcock et al. 2000), since these blazar jets are effectively point sources, but the probability of such an event should be vanishingly small) Similarly, the December 2009 flare of 3C 454.3 (Fig. 4l) moved off the standard red-bright track, although it was not as obviously achromatic.

In contrast to FSRQs, the lower luminosity BL Lac objects do not show the same color-magnitude trend, consistent with BL Lacs having weak accretion disks. The HBL PKS 2155-304 is shown in Fig. 4k; its variations are more random with respect to color, and smaller in amplitude.

Somewhat more complicated is the color behavior of the LBL OJ 287 (Fig. 4d), which shows some redder-when-brighter changes but also variations that are bluer-when-brighter, and still other color changes at fixed magnitude. One possible explanation for hybrid behavior of this kind might be that the accretion disk component in OJ 287 is variable and comparable in magnitude to the jet component. Note that this complicated color-magnitude behavior is a known phenomenon in X-ray binaries, where hysteresis in the X-ray flux–spectral index plane has been interpreted in terms of accretion state changes (Smith et al.

2007; Maccarone & Coppi 2003). Like the optical emission in LBLs and FSRQs, X-rays in X-ray binaries are thermal emission from an accretion disk. On the other hand, hysteresis behavior has also been been reported for the HBL PKS 2155-304 (Kataoka et al. 2000), in which the X-rays come from the jet (and no disk has been detected). On balance, it is not obvious what causes the unusual color-magnitude trends in OJ 287.

Still more anomalous behavior is exhibited by AO 0235+164 (Fig. 4b). At the beginning of our monitoring program, for example, increasing intensity was characterized by bluer (not redder) colors. This was also when AO 0235+164 was detected by Fermi in the daily light curve (i.e., it was gamma ray-bright, c.f. Fig. 1b). Later, when the source was much fainter in gamma rays, the color-magnitude trend reverted to the usual redder-when-brighter relation. We note that the X-ray binary GX 339-4 has been observed to change from a bluer-when-brighter state (associated with the high/soft X-ray state) to a redder-when-brighter state (associated with the hard X-ray state — see Buxton et al. 2011 submitted).

If the observed optical-IR emission is a combination of jet and accretion disk, and if the gamma rays were produced by inverse Compton scattering of disk or line photons, then the two trends can be explained self-consistently. When the jet becomes brighter, the color of the combined emission gets redder since the jet synchrotron emission is intrinsically redder than that of the blue accretion disk. Alternatively, if the jet is constant and the disk emission increases, then the summed emission becomes bluer. Moreover, an increase in disk emission would be accompanied by a strong increase in gamma rays, due to the increased scattering of disk/line photons, hence the association of a bright gamma-ray state with the bluer-when-brighter trend. In addition, when the jet is quite bright ($J \gtrsim 14$ in this case), further brightening of the jet may be due to emission from an even higher energy population of electrons; this would also result in a bluer color. 3C 279 (not shown) has a very similar (i.e., hybrid) color-magnitude diagram, roughly achromatic in the optical when bright in gamma rays but much fainter in gamma rays when it moves along the more usual FSRQ bluer-when-fainter trend.

In the examples of AO 0235+16 (Fig. 4b) and 3C 279 (Fig. 4f), different loci in the optical/IR color-magnitude diagram are associated with different gamma-ray intensities. This bimodal behavior has some similarity to the Galactic X-ray binaries. Their emission is a combination of soft X-rays from a disk and hard X-rays from a power-law component (likely from a hot corona). In the canonical "high-soft" state, the X-ray spectrum is disk-dominated and hence, softer, but the intensity is higher, while in the canonical "low-hard" state the intensity is lower but the spectrum is dominated by the power-law component, hence, harder (Remillard & McClintock 2006). There is a third so-called "very high state" in which the XRB spectrum is dominated by the power-law component at a very high intensity. For these

anomalous FSRQs, the gamma-ray bright times may correspond to the "very high state," in which case the optical emission will also be very bright and will get bluer when brighter because it is totally jet dominated.

5. The time-dependent spectral energy distribution

Figure 5 shows the variable broadband spectral energy distribution for 3C 454, with quasi-simultaneous data (within hours) for UT 2009 Dec. 03 (*blue*) and UT 2009 Dec. 04 (*red*), when the source was near the peak of its large December 2009 flare. A representative SED for a non-flaring state is shown for UT 2009 Aug. 12 when the source was relatively faint (*black*). The X-ray (*Swift* XRT and BAT) and gamma-ray (*Fermi*) data points shown are taken from the analysis in the paper of Bonoli et al. (2010). The NIR-optical points shown are the SMARTS monitoring data presented in this paper. The gamma-ray (inverse Compton) and optical-NIR spectra (presumably the high-energy end of the synchrotron emission component) both varied significantly during the 3-4 Dec 2009 flare, but in opposite senses. That is, the gamm-ray spectrum flattened and declined slightly while the optical/IR steepened and increased in flux. This definitely points to complex physical changes beyond a simple electron acceleration.

Note that the SMARTS data are extended enough in energy coverage that one can see that the synchrotron spectrum is not consistent with a power law and the synchrotron emission peak likely moved. On the other hand, if one ignored the NIR (J, K band) points, then one might conclude that not much had happened in the optical and gamma-rays, and consequently that the underlying electron energy distribution and source parameters were roughly similar. This was the conclusion of Bonoli et al. (2010), who focused on fitting the X-rays and gamma-rays and only roughly matched the optical intensity of the source. Thus the ability of SMARTS to cover both optical and IR bandpasses constrains the physical interpretation in ways that gamma-ray or optical monitoring alone does not.

If we assume the optical-NIR emission is produced in the same source region as the gamma-rays (which is not unreasonable as this is a very bright flare and the gamma-ray and optical variations are correlated), then our preliminary SED modeling of the NIR to gamma-ray data (shown by the solid red and blue curves, computed using the one zone code of Coppi 1992) indicates that the source variations must be more significant than indicated in Bonoli et al. (2010). For source parameters similar to to theirs ($R_{source} =\sim 10^{17}$cm, $\delta \sim 20$, $B \sim 1$, $\gamma_{peak} \sim 500$), we find that the electrons responsible for the optical-NIR emission are likely higher in energy than those responsible for the gamma-ray emission, and that Klein-Nishina effects are thus important for them. This means that in order to produce a *steeper* yet higher

amplitude synchrotron spectrum, the external photon field seen by the emitting electrons must have changed to include more lower-temperature photons than the BLR – see Moderski et al. (2005b) and Moderski et al. (2005a) for a discussion of the dependence of Klein-Nishina effects on the external photon field. Varying the ambient photon field alone, however, is not enough to explain all the observed spectral changes: in the context of traditional one-zone synchrotron-Compton models, some combination of peak electron energy, the magnetic field, and the Doppler beaming factor must have changed by factors of two or more.

Note also that if our preliminary conclusions are correct, namely that gamma-ray and optical emission comes from somewhat different energy electrons, and that the mapping from electron energy to synchrotron and Compton photon energy may change during the flare, then this might explain why we see general but not exact correlations between the variability in gamma-ray and lower energy bands. One-zone models may still have some relevance during bright flares, if one region of the jet dominates the overall emission. Finally, note also that the lore that Fermi spectra do not change much during flares appears to be at best a coincidence in 3C 454.3: the underlying electron and target photon spectra change significantly.

6. Conclusions

Systematic monitoring of southern blazars with the SMARTS optical+infrared ANDICAM has generated BVRJK light curves for a dozen blazars, all of which were contemporaneously observed with the Fermi gamma-ray satellite. All of the SMARTS blazar photometry is available on a publicly accessible web site, http://www.astro.yale.edu/smarts/fermi. This paper reported on the 12 blazars that have well defined optical/IR light curves over the first 2 years of the Yale/SMARTS blazar monitoring project, which commenced in August 2008.

Not all twelve blazars are significantly detected in gamma-rays on ∼day timescales. For the first two years of data (through July 2010), six SMARTS-monitored blazars were bright enough to be well detected in one-day averages at gamma-ray energies: the FSRQs 3C 454.3, 3C 273, 3C 279, and PKS 1510-089; the LBL AO 0235+164; and the HBL PKS 2155-304. Detailed multiwavelength analysis was presented for these six.

We find the optical/IR and gamma-ray light curves for these six southern blazars are generally well correlated, with lags of less than 1 day (roughly the sampling interval for the SMARTS and Fermi data). This strongly supports leptonic models in which ambient photons — perhaps from the accretion disk or broad emission-line clouds — are upscattered to gamma-ray energies by synchrotron-emitting electrons in the relativistic blazar jet. Hadronic models, in which the gamma-rays come from energetic protons that ultimately decay into

synchrotron-emitting electrons, do not have the same natural explanation for correlated optical/IR and gamma-ray variability.

The multiwavelength variability for the six blazars shows two types of behavior. In luminous blazars like FSRQs, the amplitude of optical/IR variability decreases towards shorter wavelengths, as if that wavelength range had a significant underlying contribution from a more slowly varying thermal disk peaking in the UV. In BL Lac objects, the optical/IR variability is similar in different bands, consistent with little or no contribution from a (radiatively inefficient) disk.

Color-magnitude variations in these six blazars can be explained in part by highly variable jet emission mixed with slower varying disk emission. Gamma-ray flares can result from particle acceleration in the jet or from secular increases in disk/line emission, hence the somewhat complicated trajectories of blazars in color-magnitude space. Analogous multiple-state behavior has been observed in Galactic X-ray binaries. Meanwhile, individual jet flares in a given source can also follow different color-color tracks because of, e.g. standing shocks in different parts of the jet

The best-studied blazar, the FSRQ 3C 454.3, has had a strong flare in each year of SMARTS-*Fermi* monitoring. Its optical/IR and gamma-ray light curves are well correlated, with no measureable lag longer than one day. Its broad-band SED in the bright state is well fit by an external Compton model; in its faint state, the disk contributes more light and the SED is flatter. Day-to-day changes are difficult to explain with a simple one-zone model unless there are large changes (factors of two or more) in Doppler factor, electron energy, and/or magnetic field. More generally, our simple analysis of the 3C 454.3 SED suggests that optical/IR radiation comes from slightly higher energy electrons than the GeV gamma rays, and that Klein-Nishina effects are important in shaping both SED components.

SMARTS monitoring of southern blazars continues, with the goal of producing additional rich multiwavelength data sets that will advance our further understanding of blazar emission mechanisms and energy transport.

SMARTS observations of LAT-monitored blazars are supported by Fermi GI grant 011283 and by Yale University. CDB, MMB and the SMARTS 1.3m observing queue receive support from NSF grant AST-0707627. RC is supported by Fermi GI grant NNX09AR92G. GF is supported by Fermi GI grant NNX10A042G. JI is supported by the NASA Harriet Jenkins Fellowship program and NSF Graduate Research Fellowship under Grant No DGE-0644492. This research has made use of the NASA/IPAC Infrared Science Archive, which is operated by the Jet Propulsion Laboratory, Californina Institute of Technology, under contract with the National Aeronautics and Space Administration.

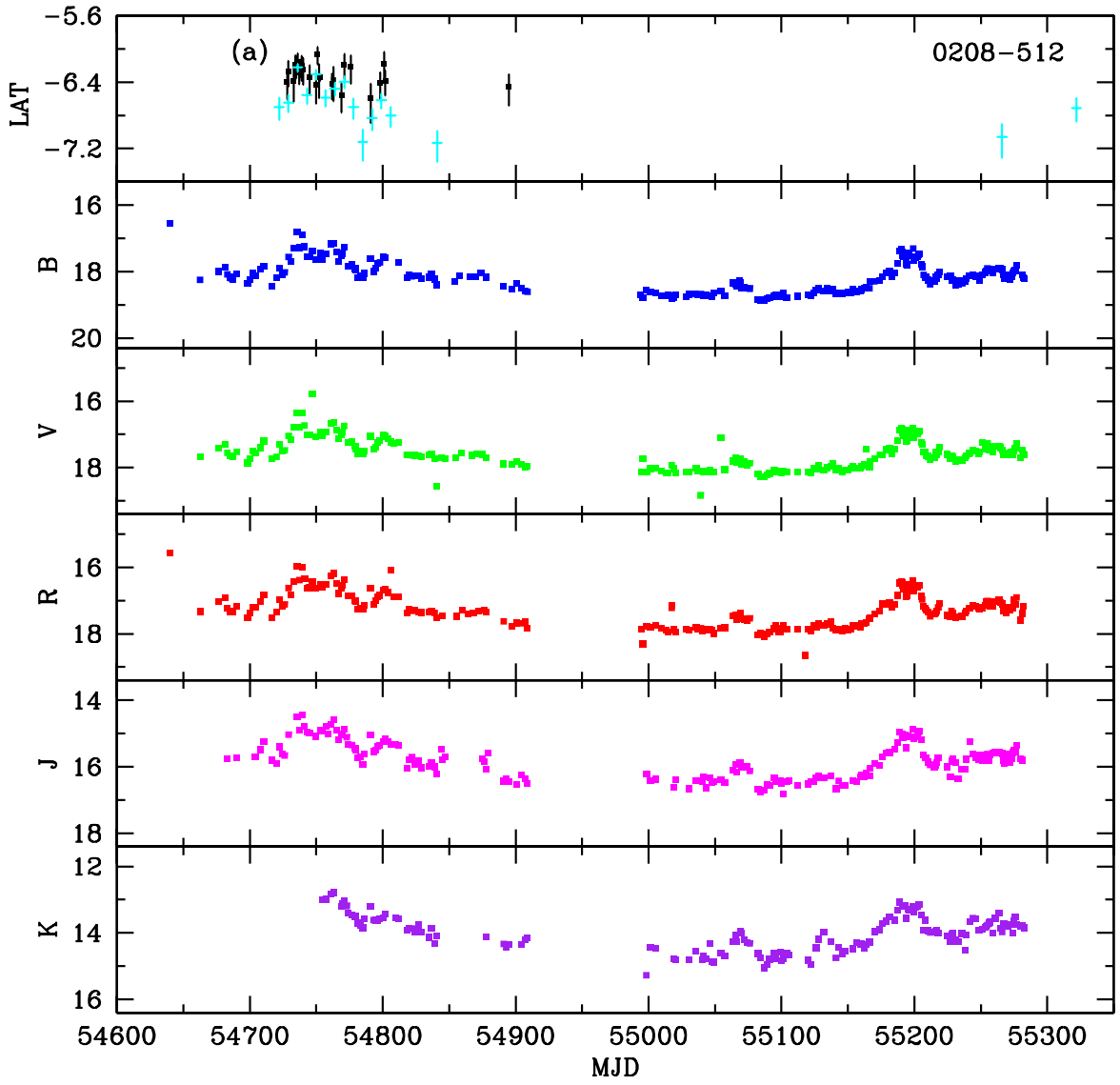

Figure 1a: SMARTS optical and near-infrared light curves for PKS 0208-512. *Fermi*/LAT fluxes are taken from the public daily (black points) and weekly (cyan points) light curves and are in units of log (photons sec^{-1} cm^{-2})

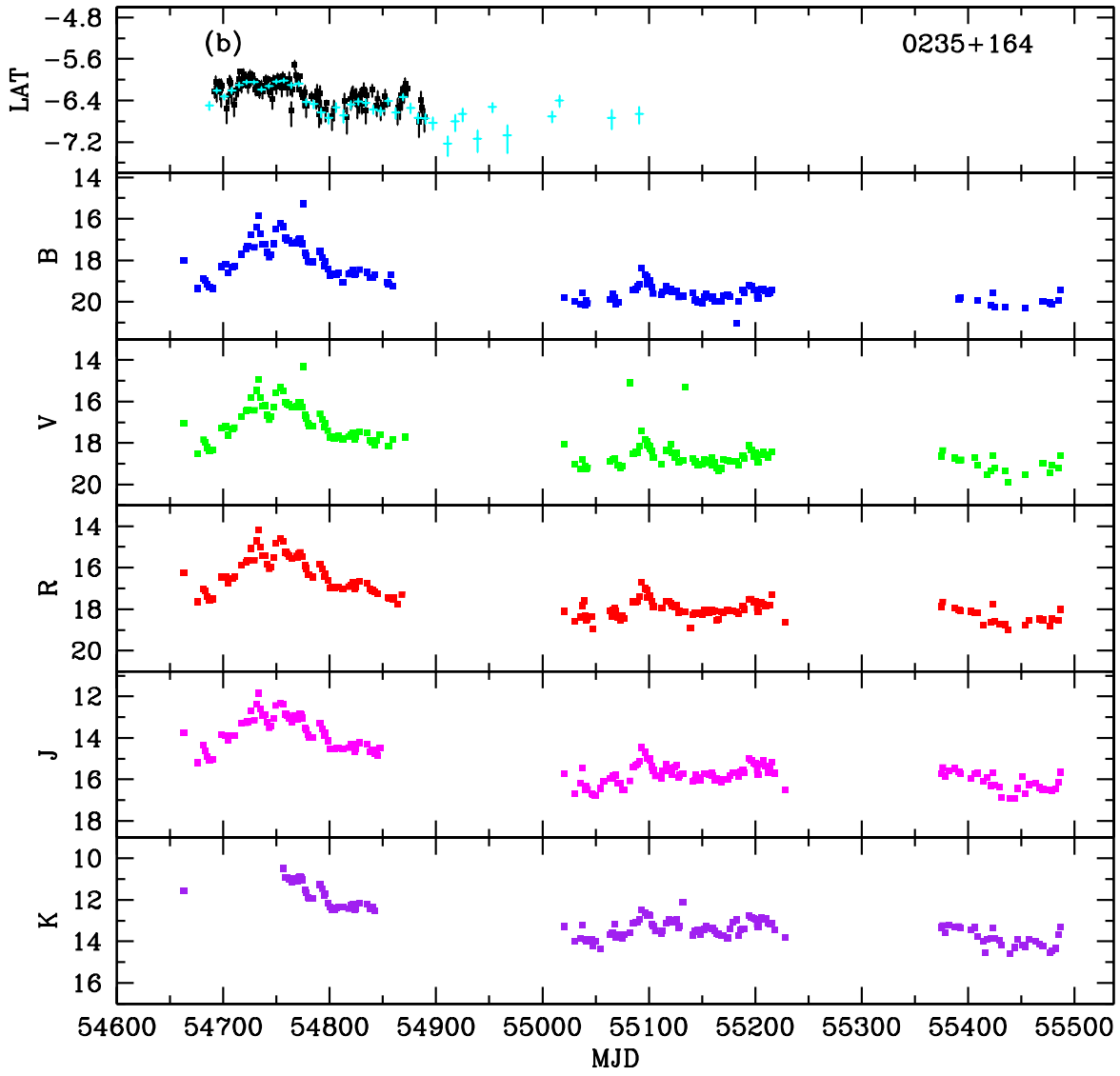

Figure 1b: SMARTS optical and near-infrared light curves for PKS 0235+164. *Fermi*/LAT fluxes are taken from the public daily (black points) and weekly (cyan points) light curves and are in units of log (photons sec^{-1} cm^{-2})

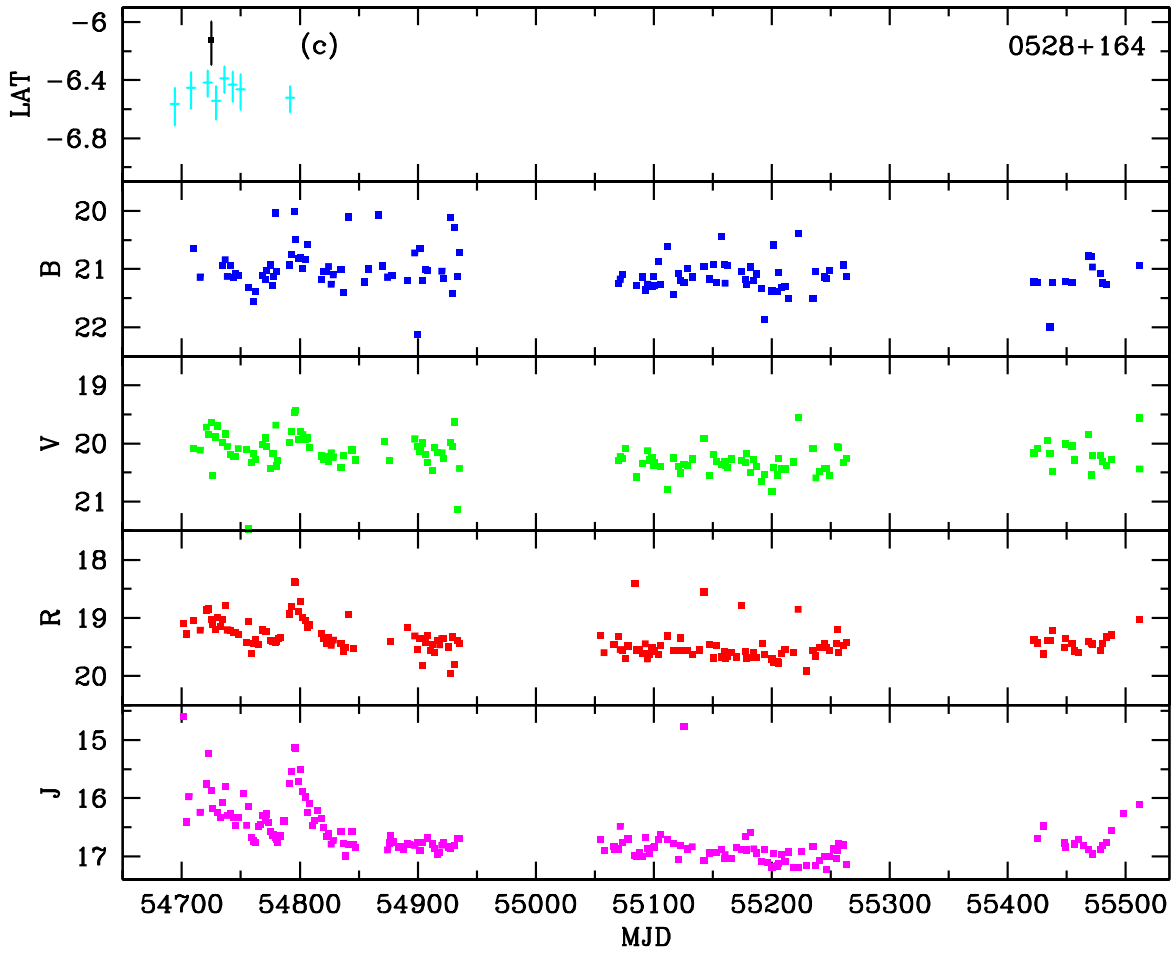

Figure 1c: SMARTS optical and near-infrared light curves for PKS 0528+134. *Fermi*/LAT fluxes are taken from the public daily (black point) and weekly (cyan points) light curves and are in units of log (photons sec^{-1} cm^{-2})

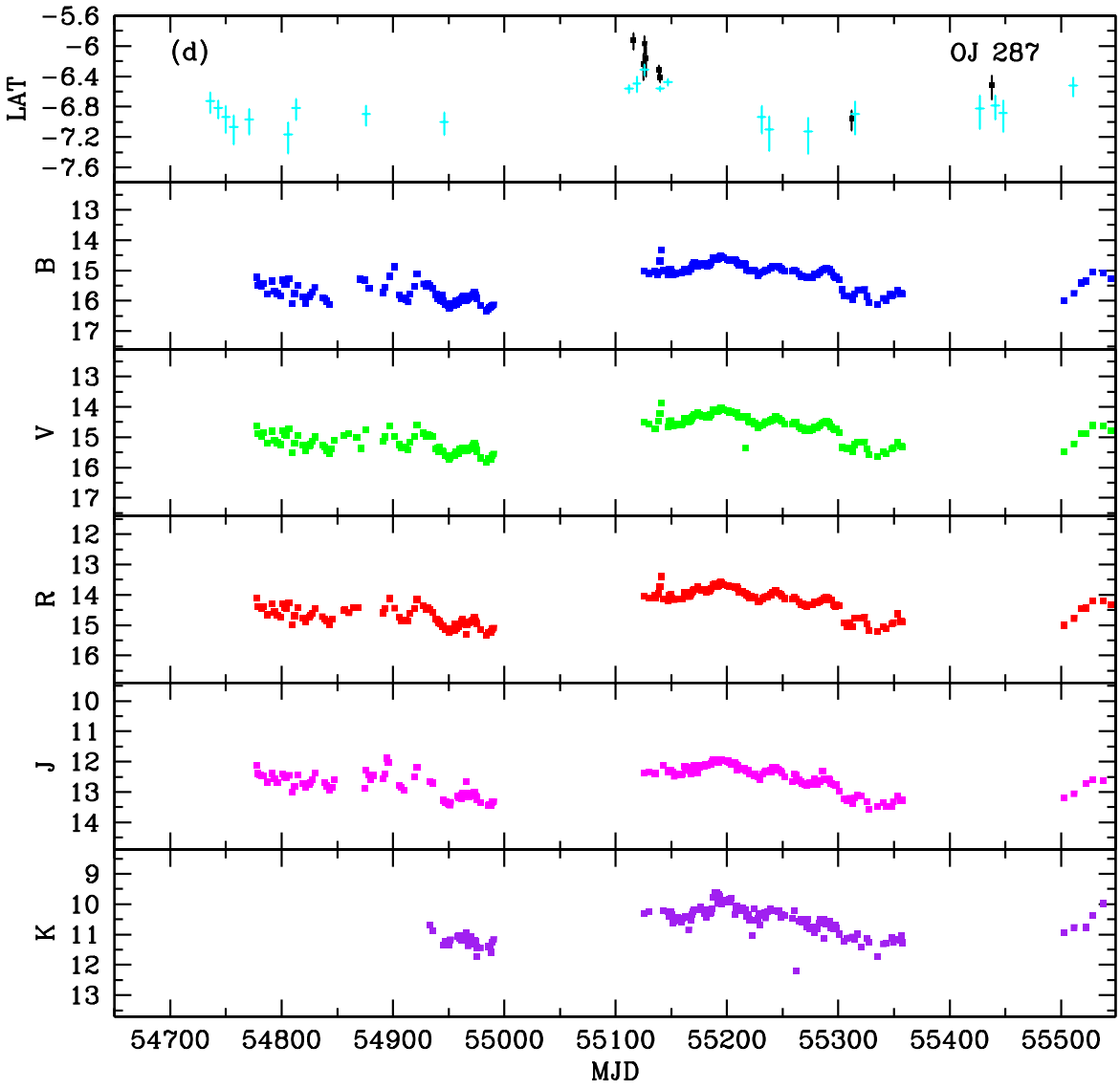

Figure 1d: SMARTS optical and near-infrared light curves for OJ 287. *Fermi*/LAT fluxes are taken from the public daily (black points) and weekly (cyan points) light curves and are in units of log (photons sec^{-1} cm^{-2})

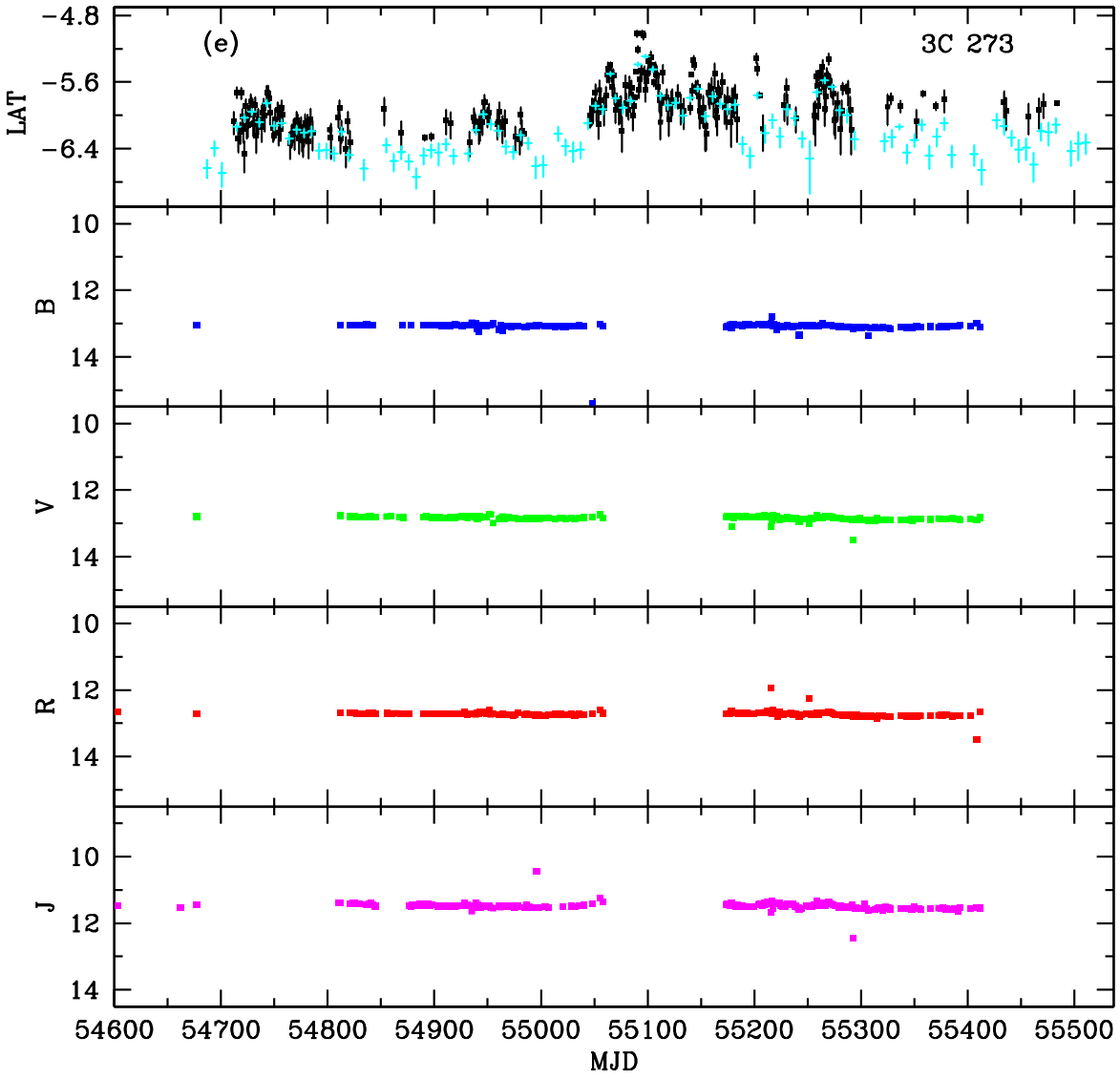

Figure 1e: SMARTS optical and near-infrared light curves for 3C 273. *Fermi*/LAT fluxes are taken from the public daily (black points) and weekly (cyan points) light curves and are in units of log (photons sec^{-1} cm^{-2})

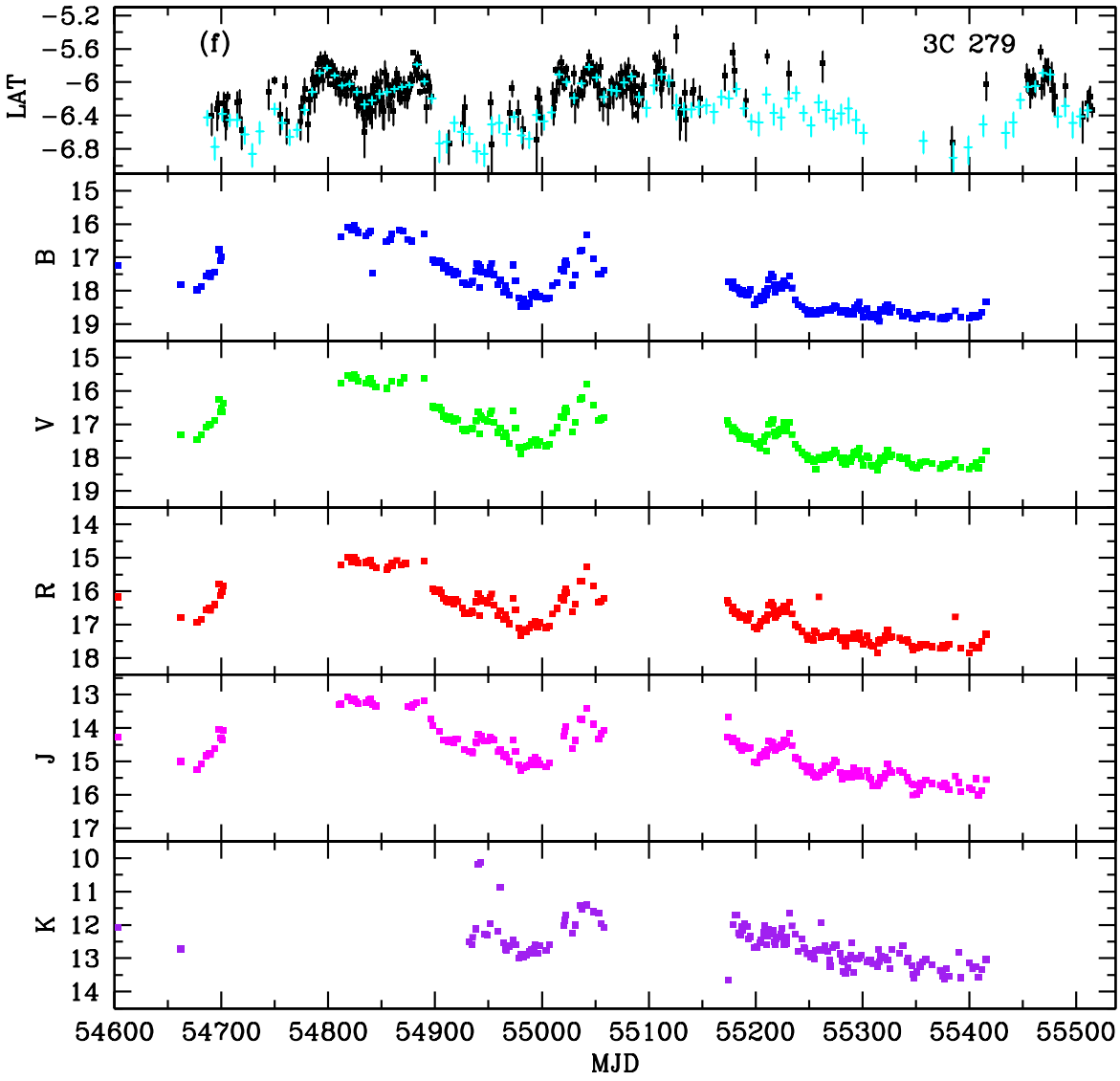

Figure 1f: SMARTS optical and near-infrared light curves for 3C 279. *Fermi*/LAT fluxes are taken from the public daily (black points) and weekly (cyan points) light curves and are in units of log (photons sec^{-1} cm^{-2})

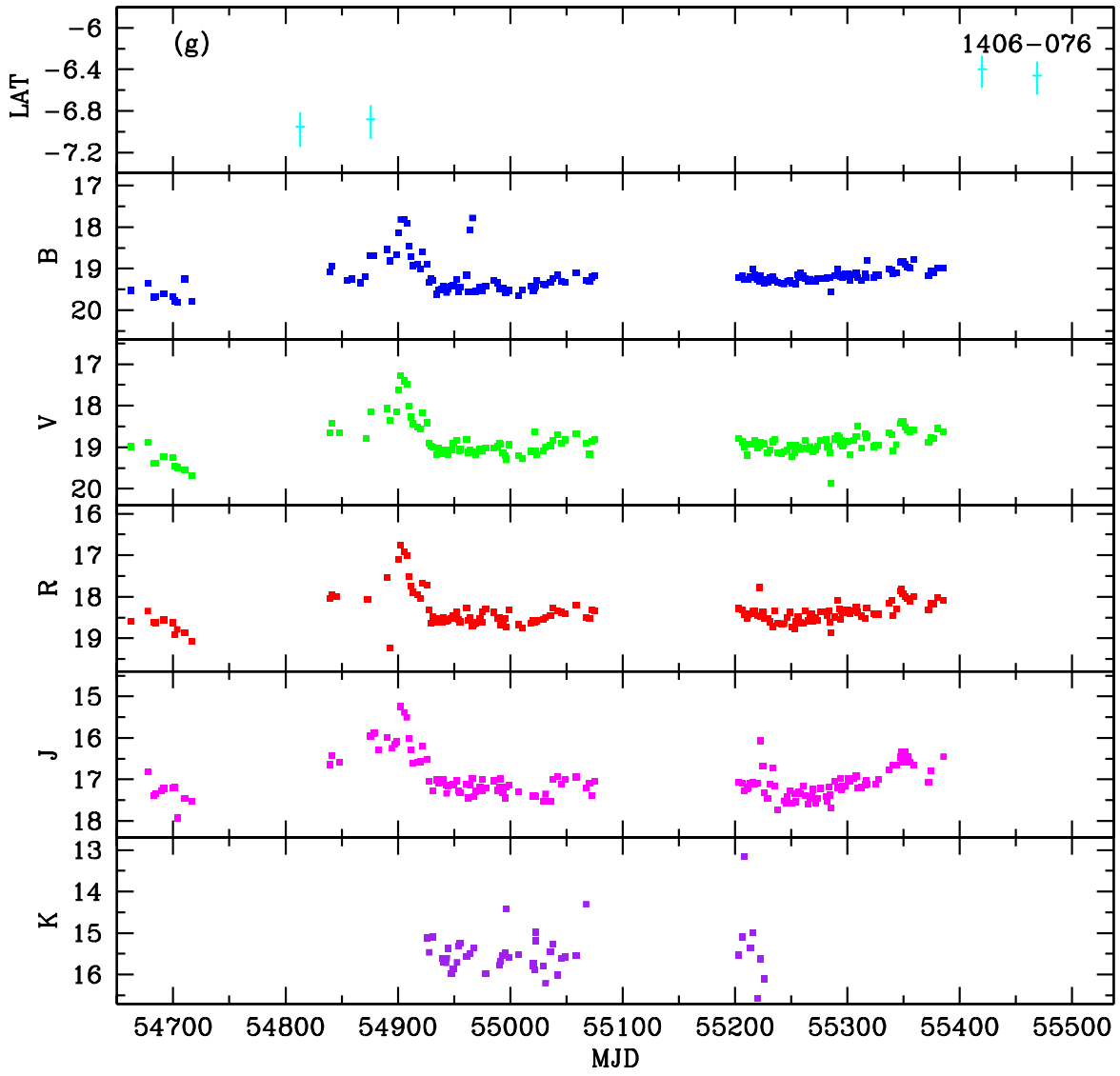

Figure 1g: SMARTS optical and near-infrared light curves for PKS 1406-076. *Fermi*/LAT fluxes are taken from the public weekly (cyan points) light curves and are in units of log (photons sec^{-1} cm^{-2})

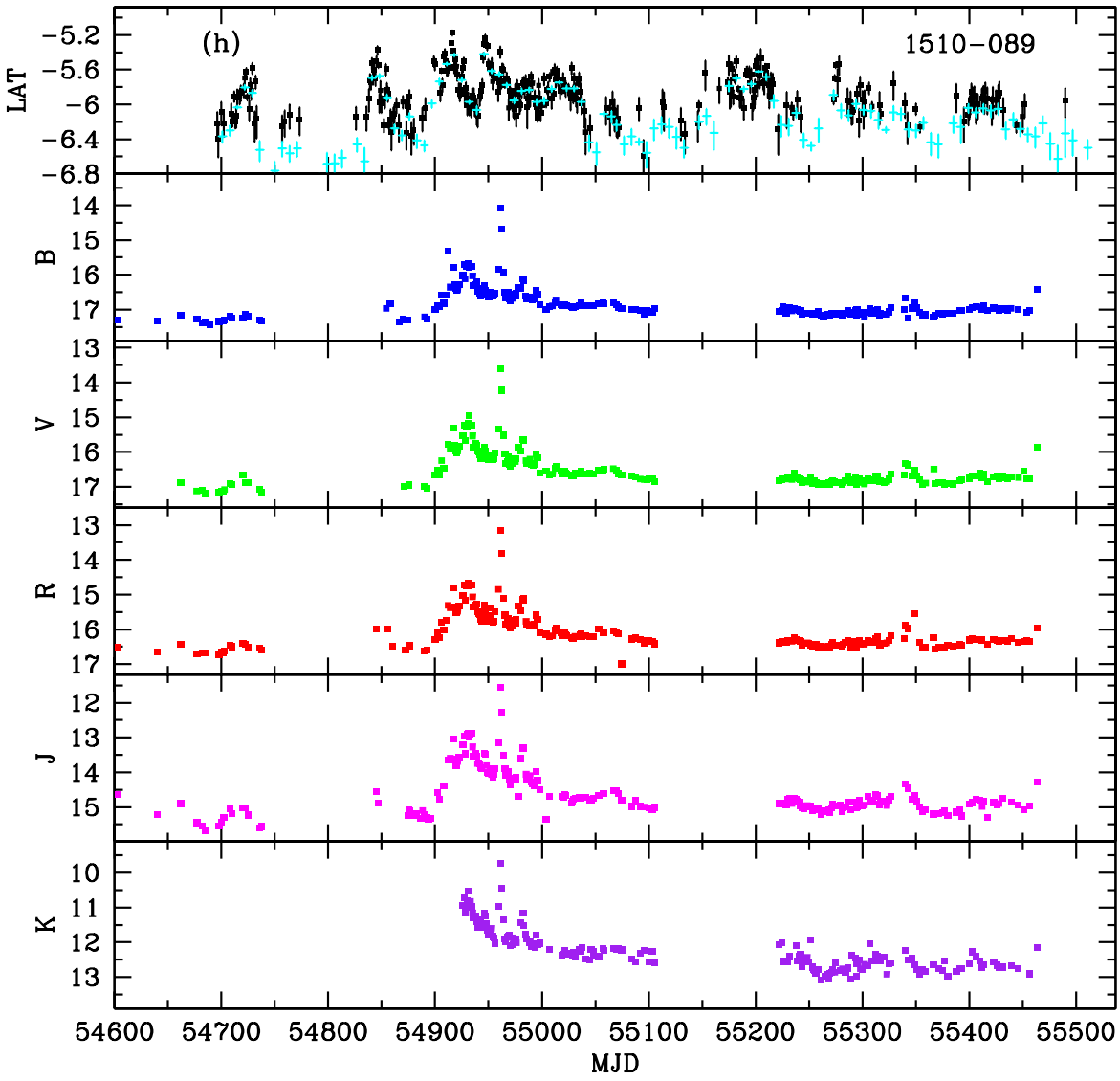

Figure 1h: SMARTS optical and near-infrared light curves for PKS 1510-089. *Fermi*/LAT fluxes are taken from the public daily (black points) and weekly (cyan points) light curves and are in units of log (photons sec^{-1} cm^{-2})

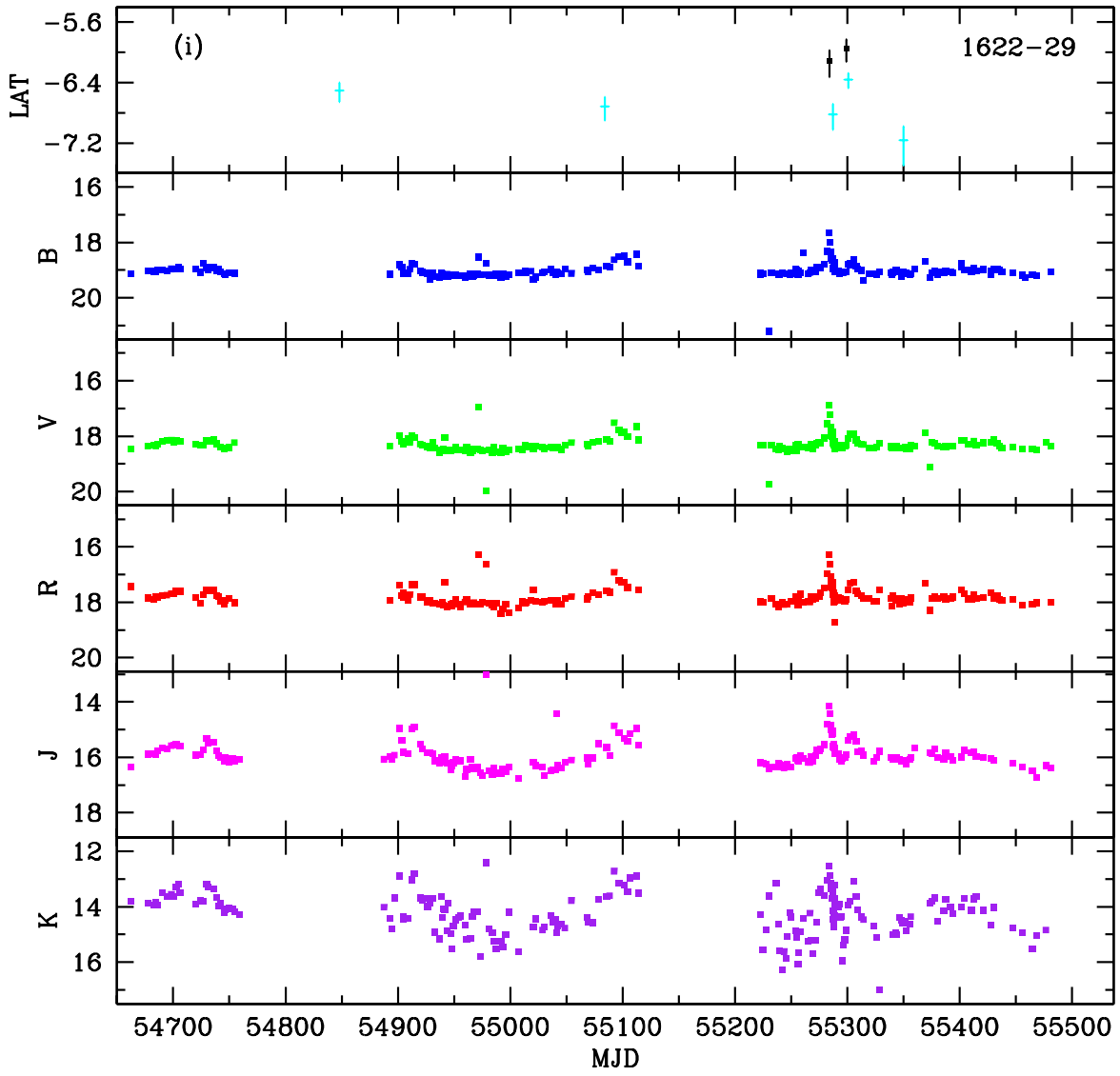

Figure 1i: SMARTS optical and near-infrared light curves for PKS 1622-297. *Fermi*/LAT fluxes are taken from the public daily (black points) and weekly (cyan points) light curves and are in units of log (photons sec^{-1} cm^{-2})

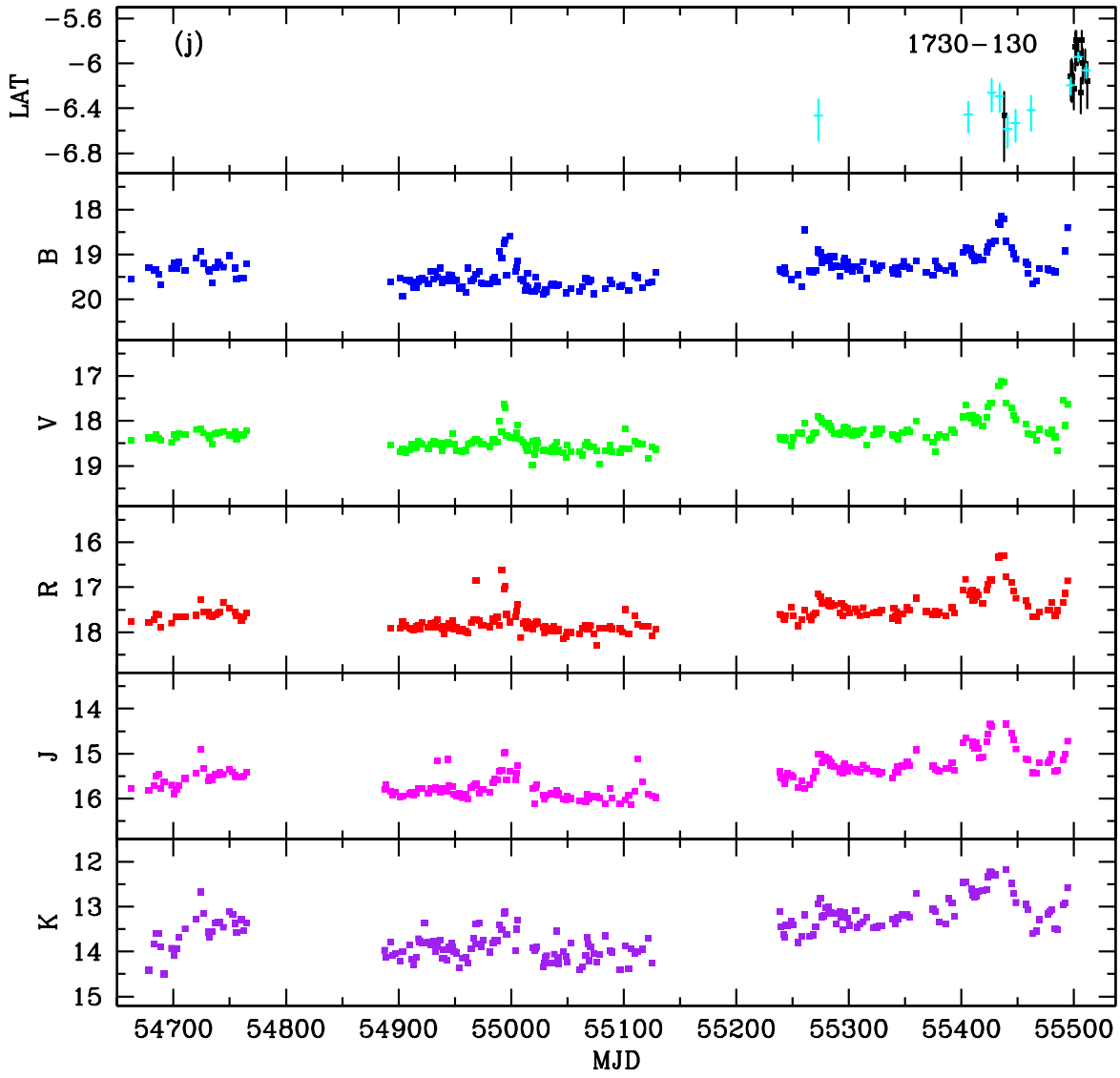

Figure 1j: SMARTS optical and near-infrared light curves for PKS 1730-130. *Fermi*/LAT fluxes are taken from the public daily (black points) and weekly (cyan points) light curves and are in units of log (photons sec^{-1} cm^{-2})

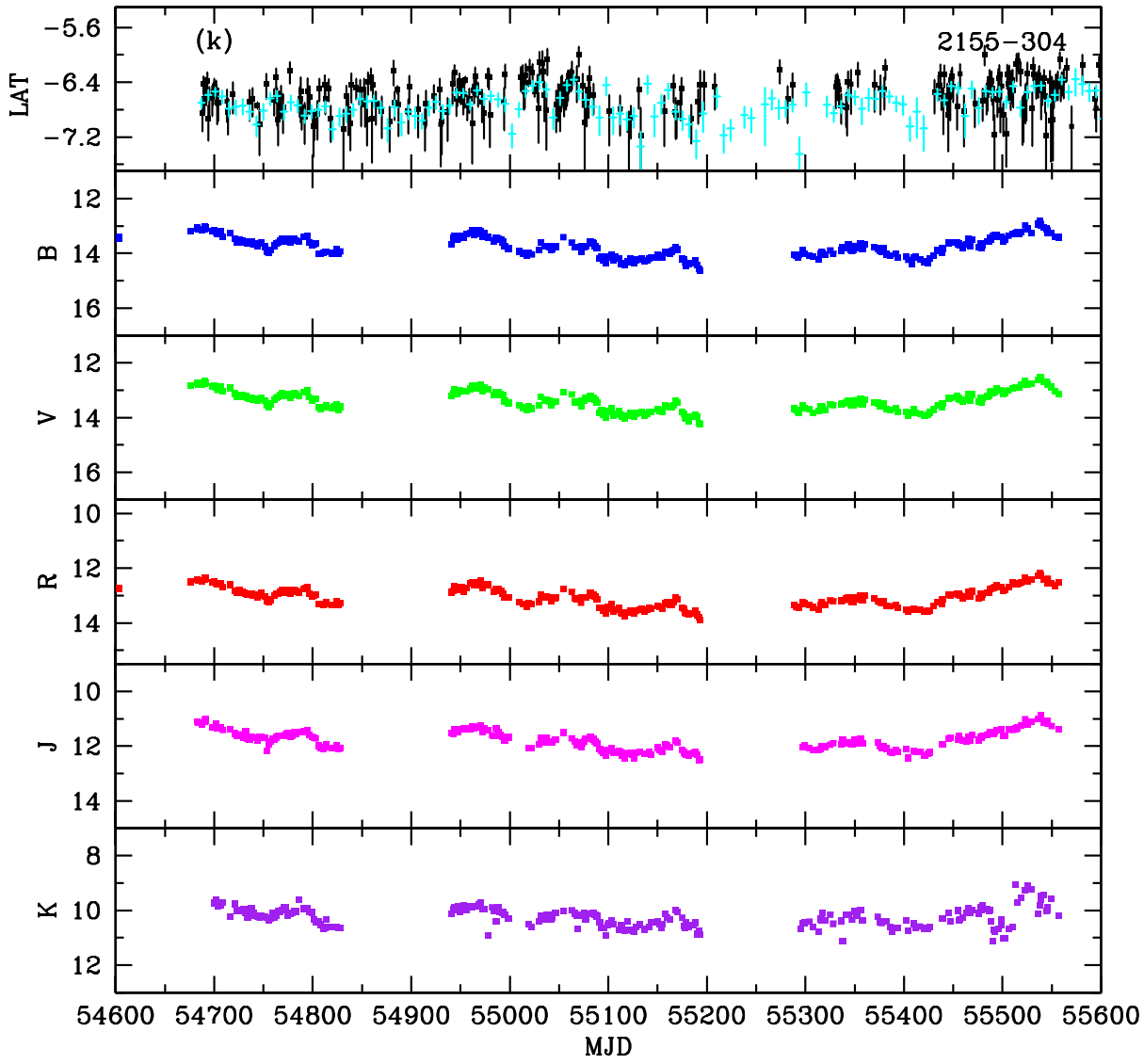

Figure 1k: SMARTS optical and near-infrared light curves for PKS 2155-304. *Fermi*/LAT fluxes are taken from the public daily (black points) and weekly (cyan points) light curves and are in units of log (photons sec^{-1} cm^{-2})

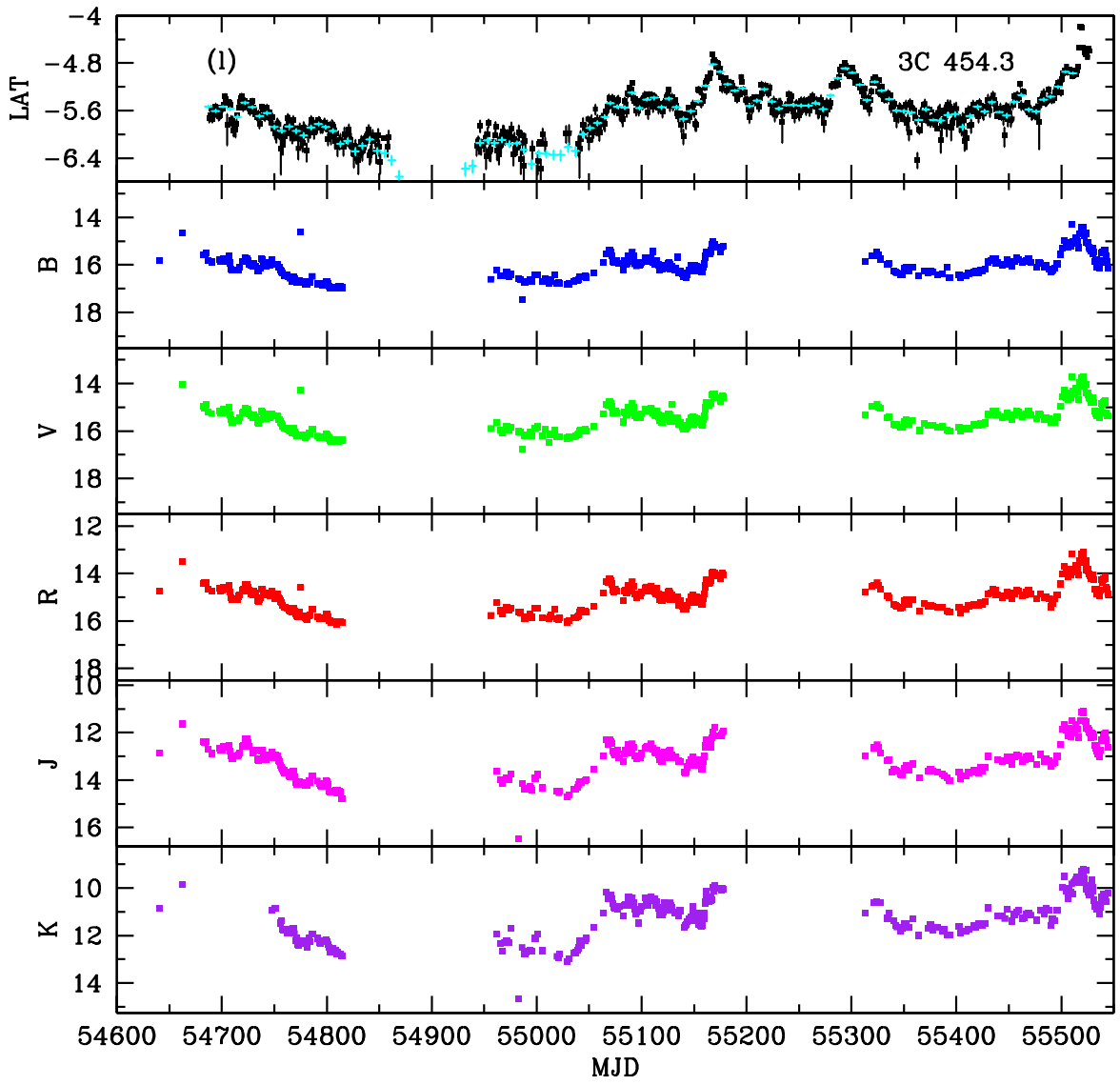

Figure 1l: SMARTS optical and near-infrared light curves for 3C 454.3. *Fermi*/LAT fluxes are taken from the public daily (black points) and weekly (cyan points) light curves and are in units of log (photons sec^{-1} cm^{-2})

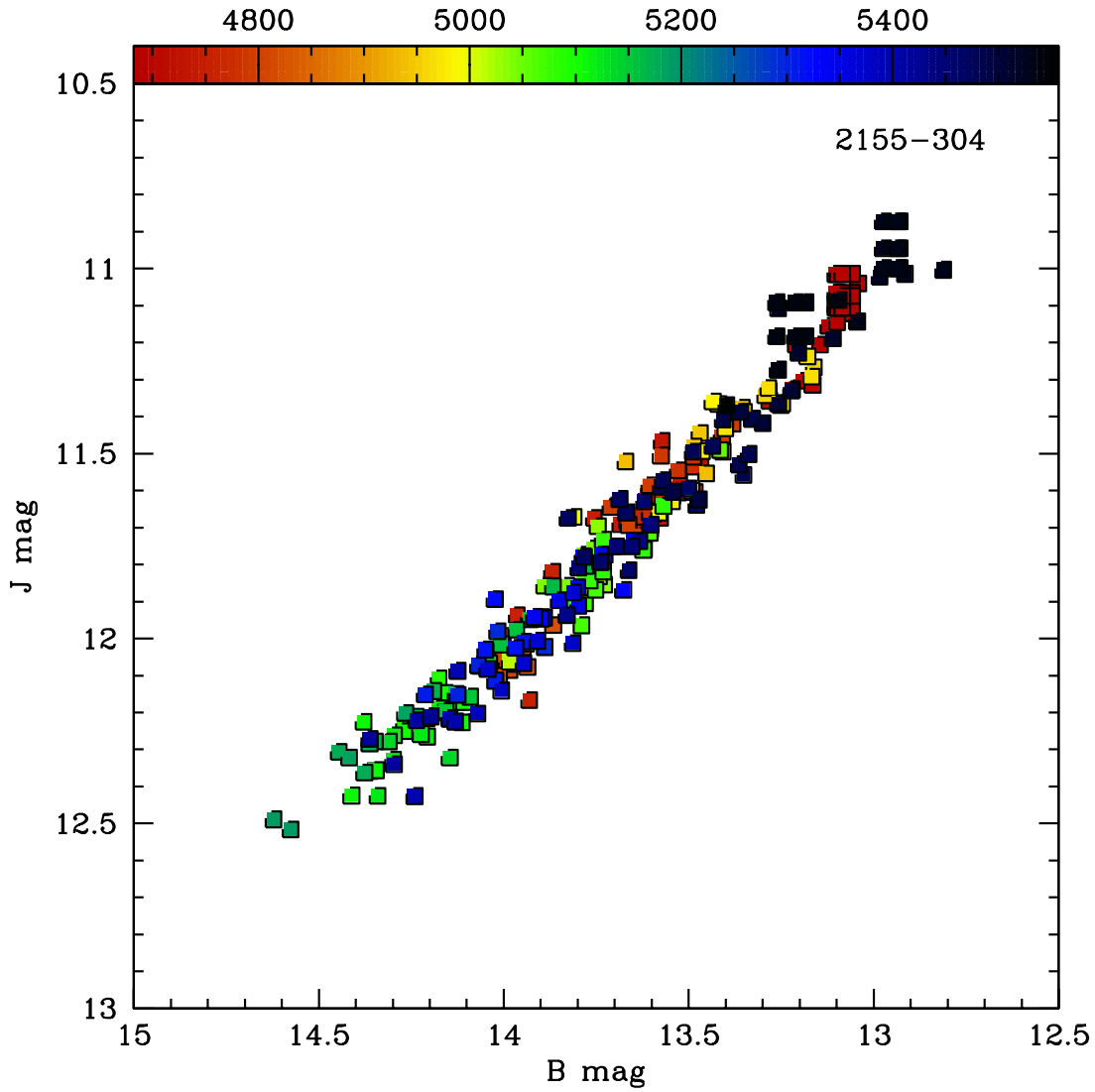

Fig. 2a: J-band vs B-band magnitude for the HBL PKS 2155-304. Color indicates the date of the observation, as shown in the top bar in MJD-50000. The tight correlation indicates that the optical and infrared emission vary together, with no significant delay.

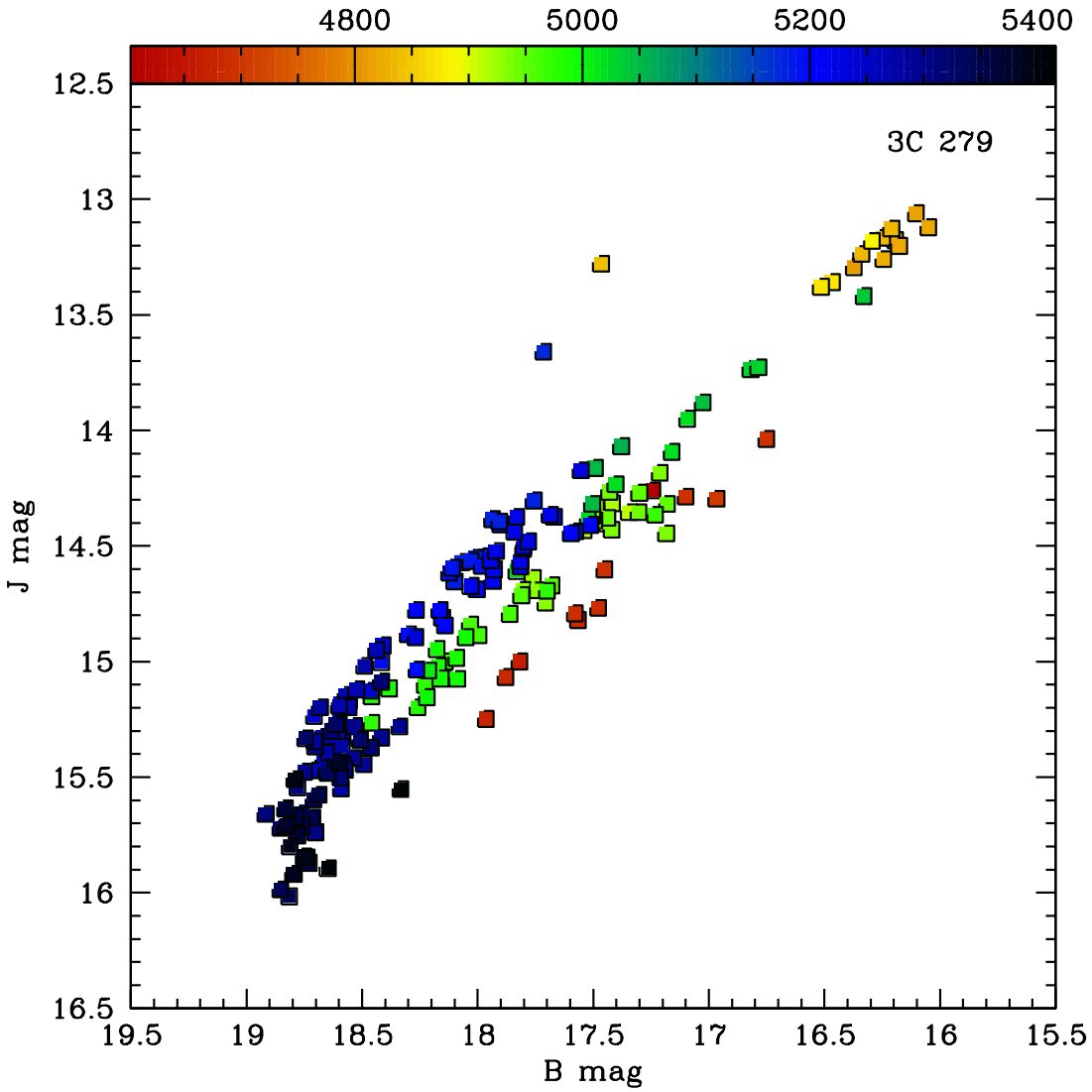

Fig. 2b: J-band vs B-band magnitude for the luminous FSRQ 3C 279. Color indicates the date of the observation, as shown in the top bar in MJD-50000. As in all sources observed, optical and infrared emission varies together. The distinct tracks for the red, green, and blue reflect changes optica/IR spectral shape over time (*c.f.* Fig. 5b).

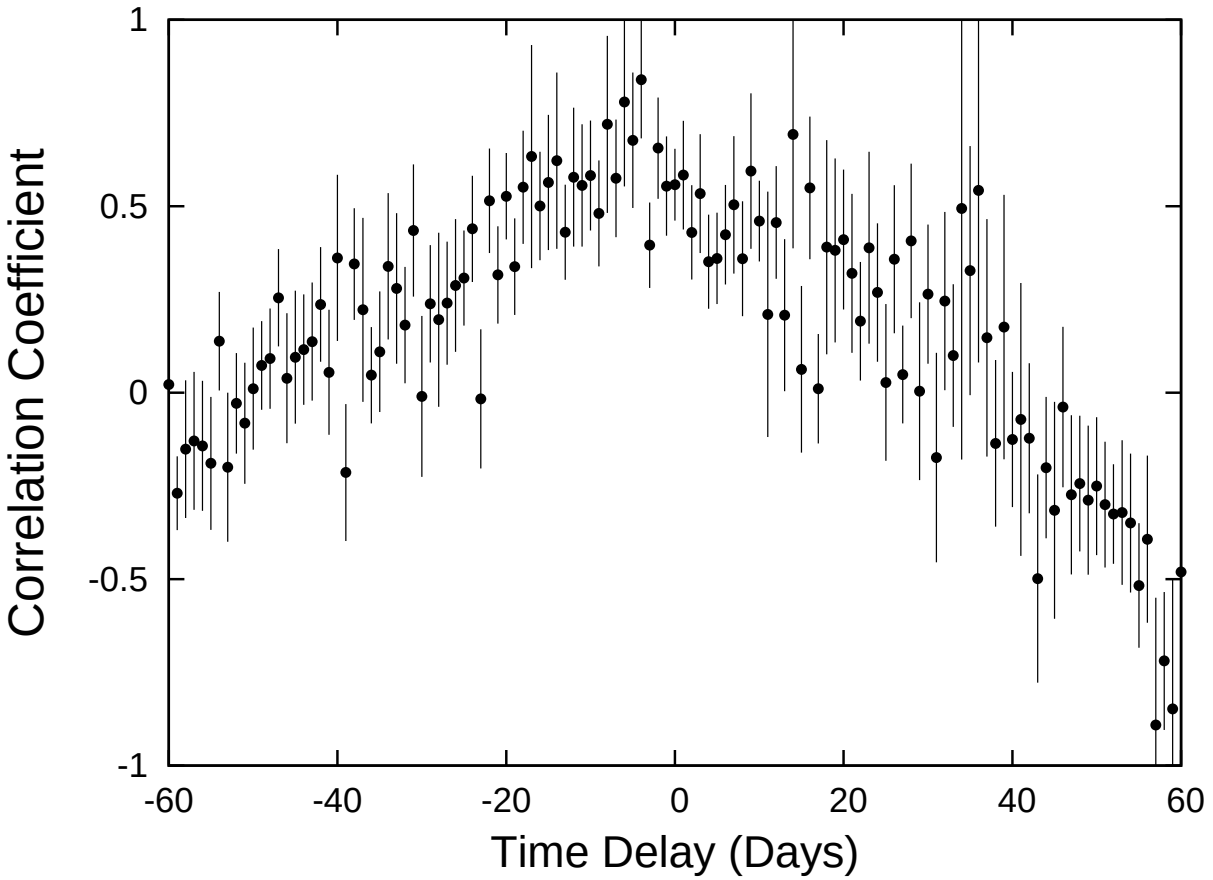

Fig. 3: The discrete cross-correlation function (Edelson & Krolik 1988) between J-band and Fermi LAT 0.1-300 GeV fluxes for the blazar AO 0235+164 shows a high degree of correlation that peaks near zero lag but is very broad. 3C 454.3 was brighter and more variable so its DCF is more strongly peaked at zero lag (Bonning et al. 2009); 1510-089 would be very strongly peaked at zero lag but for the anomalous monochromatic flare occuring in May 2010 (Marscher et al. 2010, MJD 54962,). In any case, for AO 0235+164, the duration of continuous SMARTS monitoring in this case is 200 days, in two different years, so it is not surprising that the width of the correlation when it crosses zero corresponds to about 1/3 of the length of the light curve; that is, the longest observed (though not significant) time scale is usually 1/3 of the duration of a light curve (Scargle 1981).

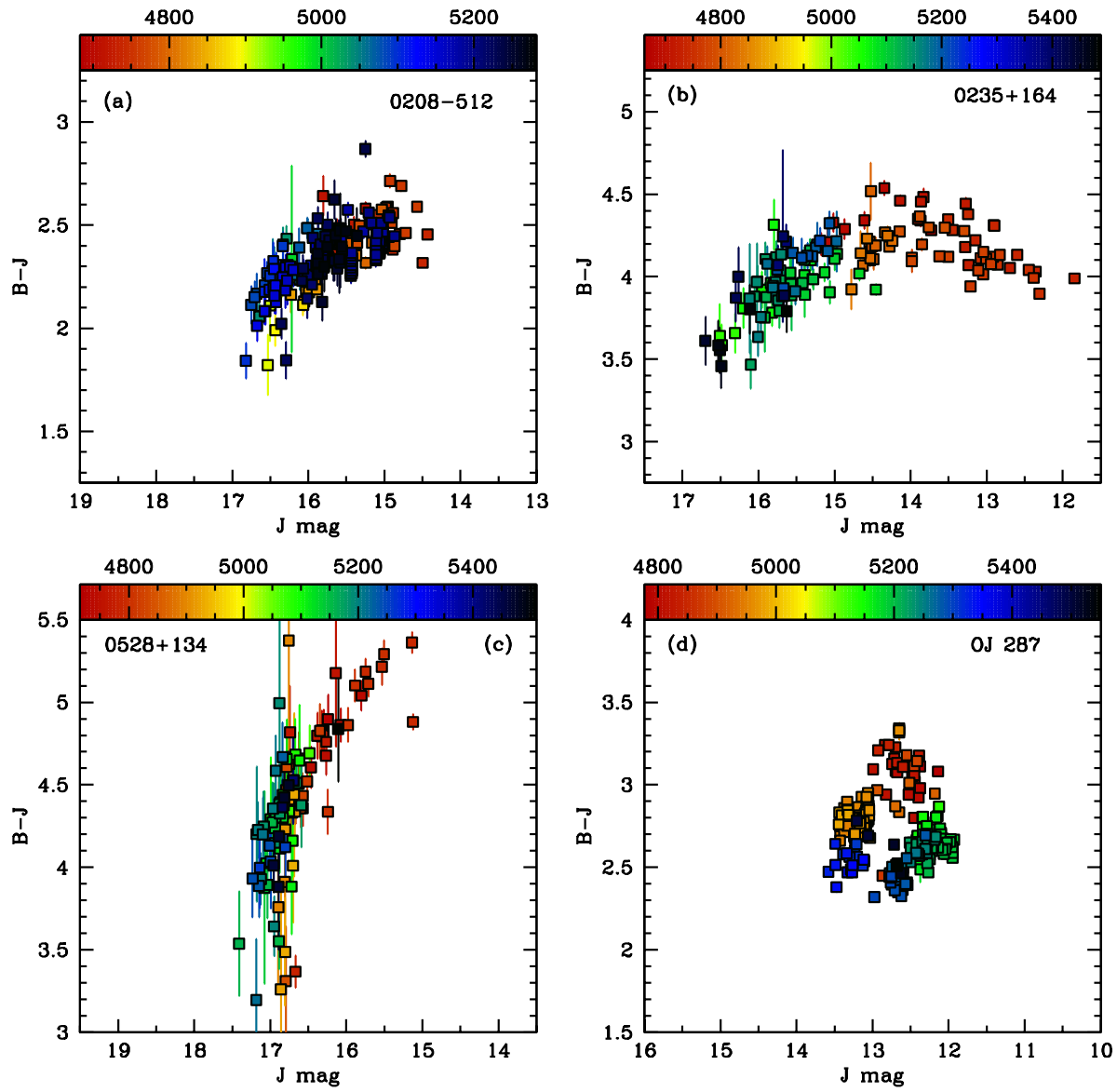

Fig. 4: $(B-J)$ color vs. J-band magnitude for FSRQs PKS 0208-512 and PKS 0528+134, and low-frequency peaked BL Lac objects AO 0235+164 and OJ 287. Color indicates the date of the observation, as shown in the top bar in MJD-50000. The FSRQs show an overall tendancy to become bluer when fainter, which suggests the presence of a steady blue accretion disk component underlying the jet emission. The two LBLs show more complicated behavior: AO 0235+164 shows some redder-when-brighter trend (blue-black points) but at early times (red-orange points) shows almost the opposite trend, getting bluer when brighter. During this bluer-when-brighter period, AO 0235+164 was very bright in gamma-rays and was easily detected by Fermi on daily time scales. When AO 0235+164 became fainter in the optical and was not detected in the daily LAT light curve, it shifted to the "normal" (for FSRQs) bluer-when-fainter trend. OJ 287 tends to move around on a circular locus in color-magnitude space where trends with brightness (including gamma-ray intensity) are not as easily definable.

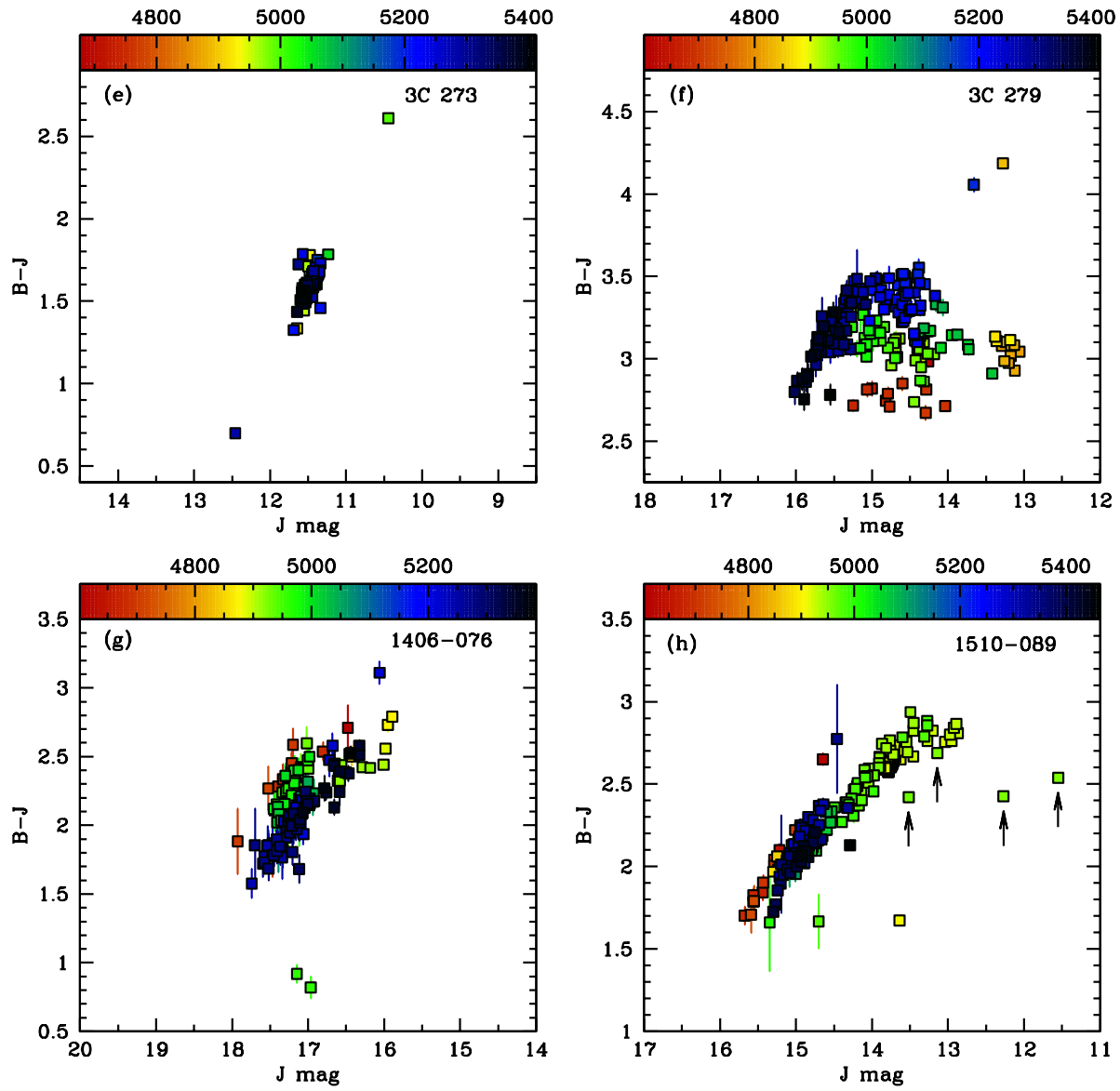

Fig. 4 (cont'd): $(B-J)$ color vs. J-band magnitude for FSRQs 3C 273, 3C 279, PKS 1406-076, and PKS 1510-089. Color indicates the date of the observation, as shown in the top bar in MJD-50000. All FSRQs show the overall redder-when-brighter (bluer-when-fainter) trend, consistent with a steady blue accretion disk component underlying the jet emission. Individual flares can behave differently, for example, the flare in PKS 1510-089 in May 2010 is achromatic (arrows indicate the 4 green points tracing a horizontal trend). The quasar 3C 279 shows compound behavior similar to AO 0235+164 (Fig. 4b), with the red-light green points tracing a horizontal loop in the color-magnitude figure before and just up to a period of bright gamma-ray activity (c.f. Fig. 1f).

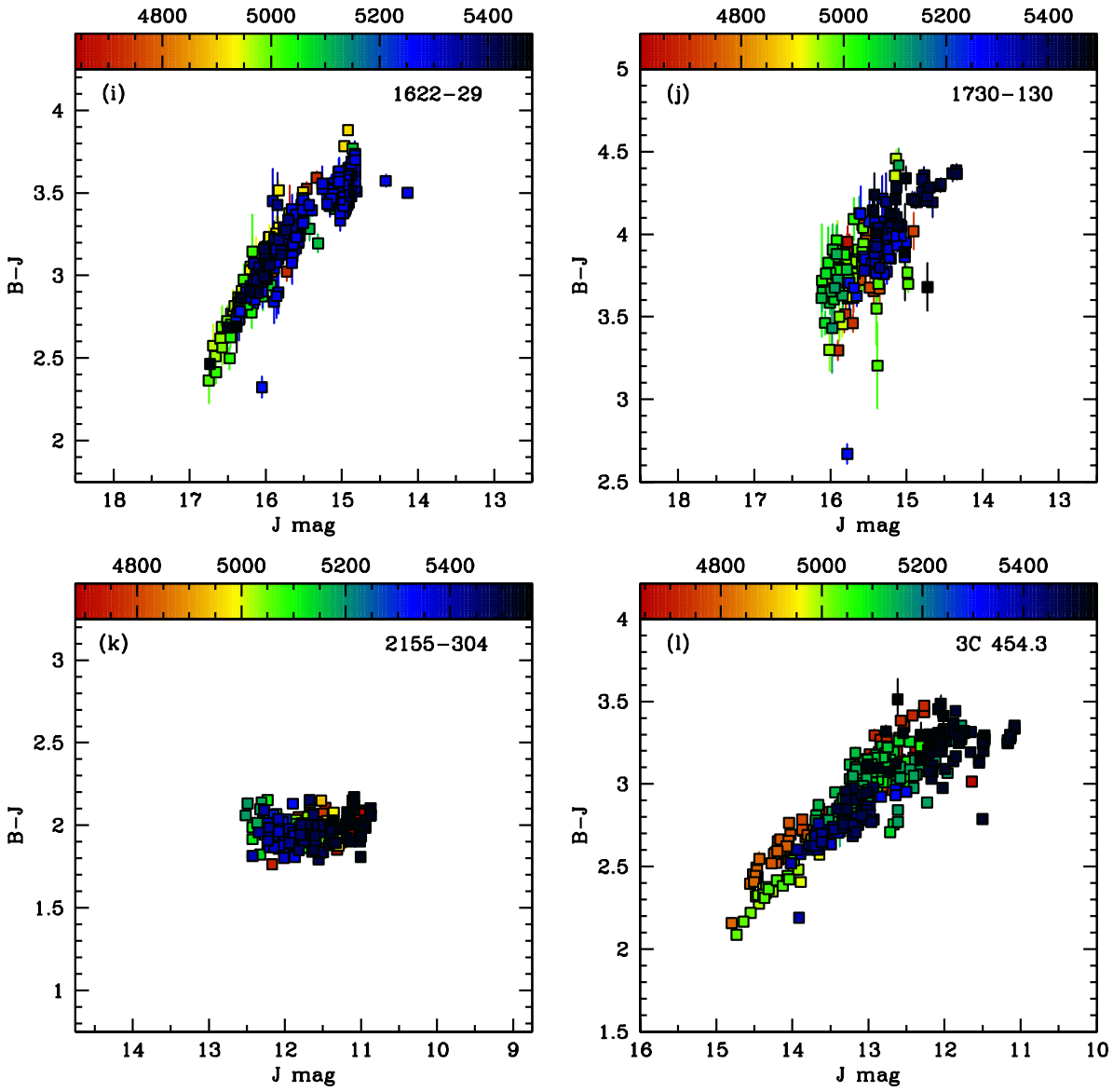

Fig. 4 (cont'd): $(B-J)$ color vs. J-band magnitude for FSRQs PKS 1622-29, PKS 1730-130, and 3C 454.3, and the HBL PKS 2155-304. Color indicates the date of the observation, as shown in the top bar in MJD-50000. FSRQs show the redder-when-brighter trend. However, for the HBL, the brightness and spectral changes are relatively small, and there is no trend of color with magnitude. This may be because the HBL both lacks a luminous accretion disk and the optical jet emission in this object is below the synchrotron peak, thus optically thick and not highly variable.

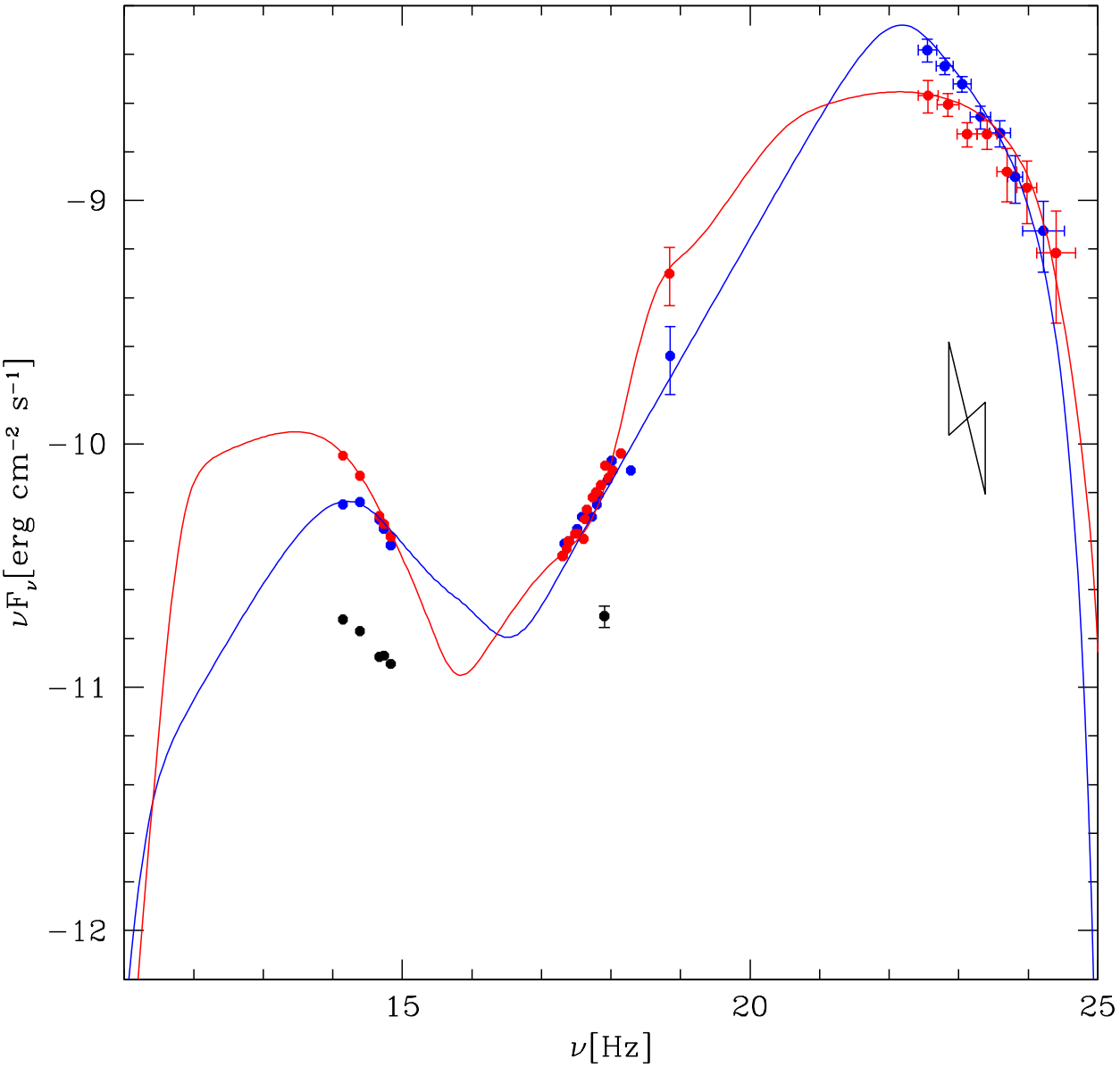

Fig. 5: Spectral energy distribution of 3C 454.3 from data obtained during the bright flare on UT Dec 03, 2009 (*blue points*) and UT Dec 04, 2009 (*red points*, and in a low state on UT Aug 12, 2009 (black points).. Blue and red *lines* are model fits to the entire dataset using the one-zone code of Coppi (1992).

A. Optical Finding Charts

We present optical finding charts for each of the 12 SMARTS-monitored blazars discussed in this paper. All figures are V-band. Field of view is approximately $6' \times 6'$. North is at top of image, East is to the left. Comparison stars are numbered; calibrated magnitudes for our comparison stars are given in Appendix C.

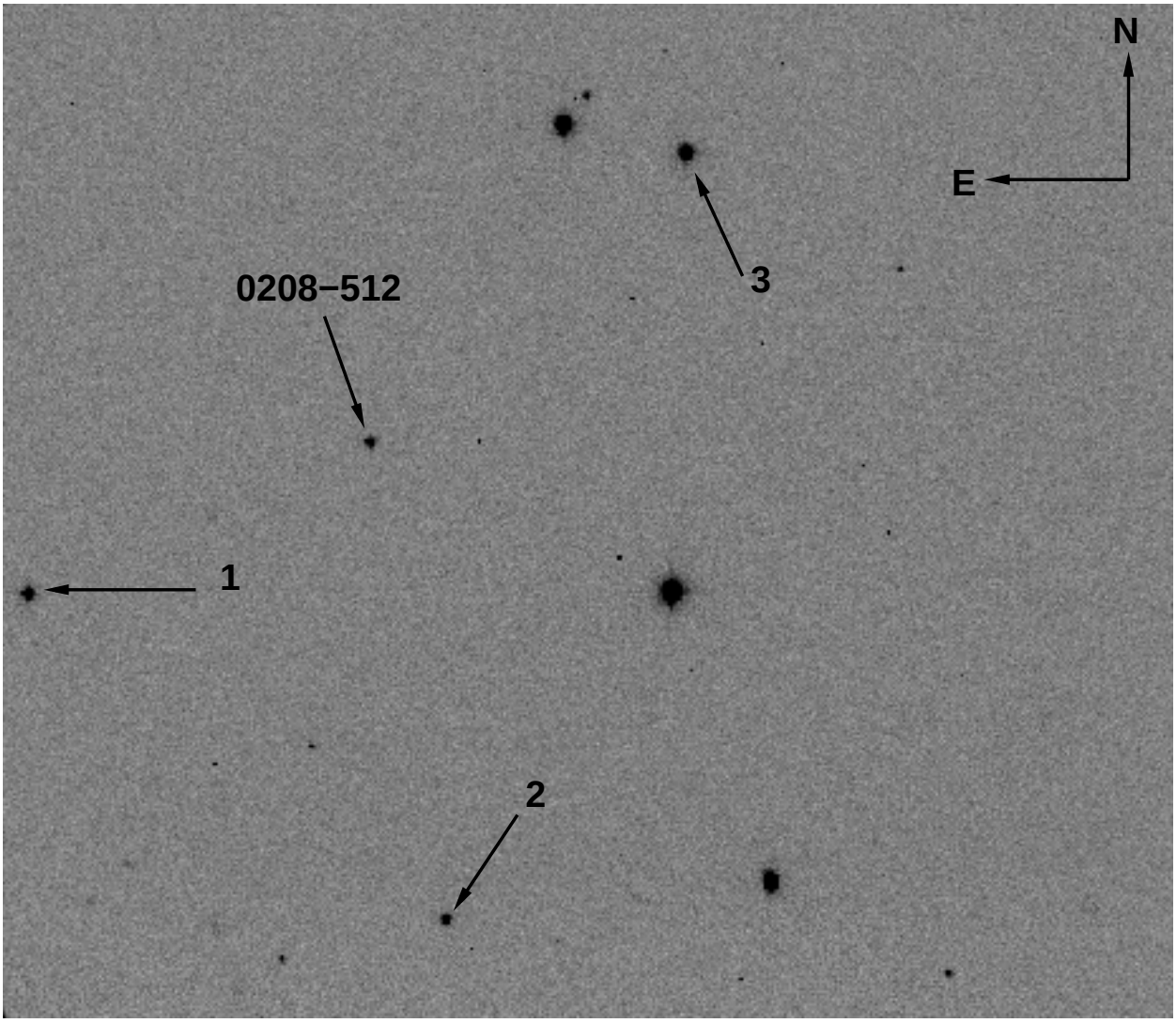

A.1: PKS 0208−512.

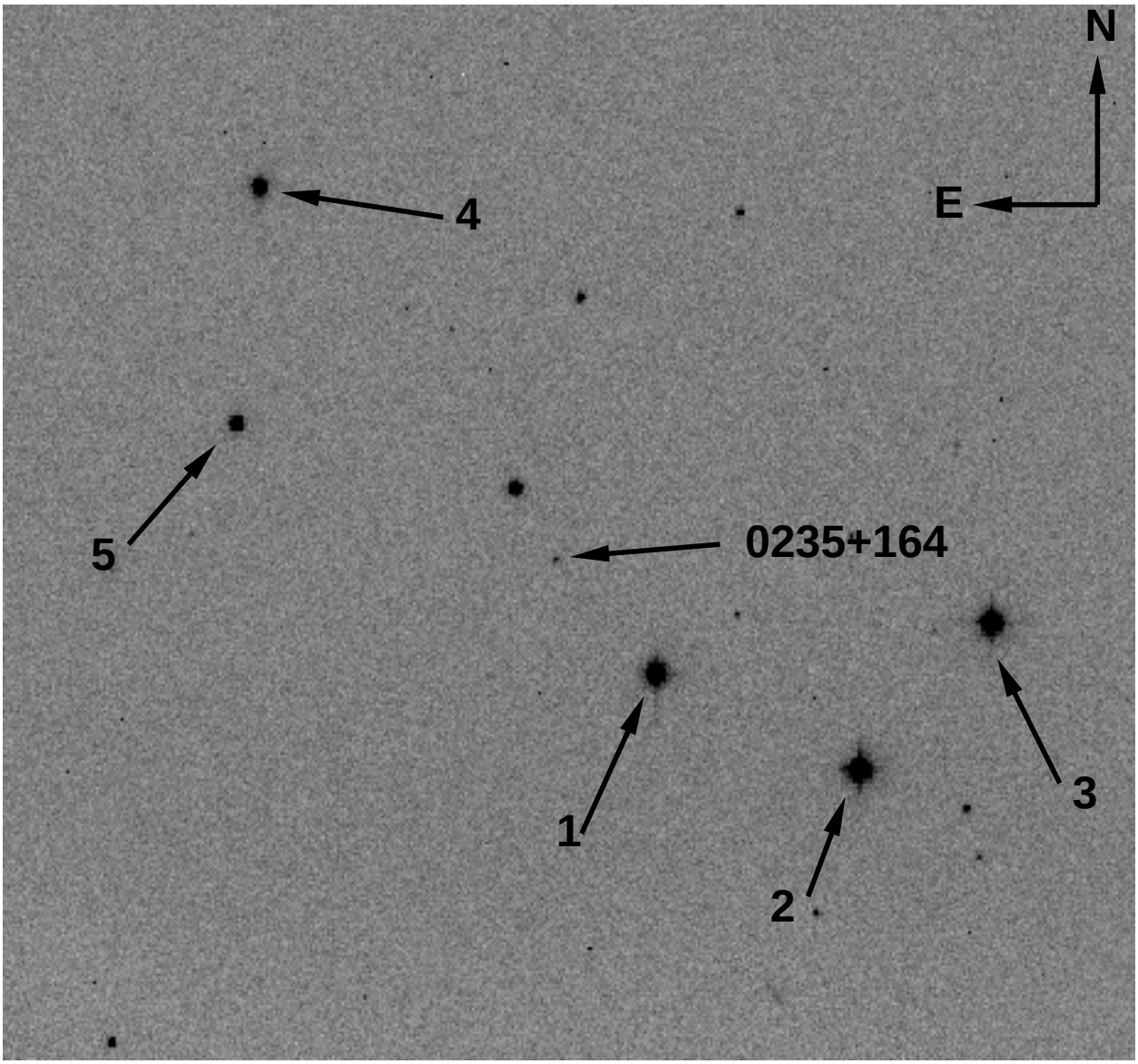

A.2: AO 0235+164.

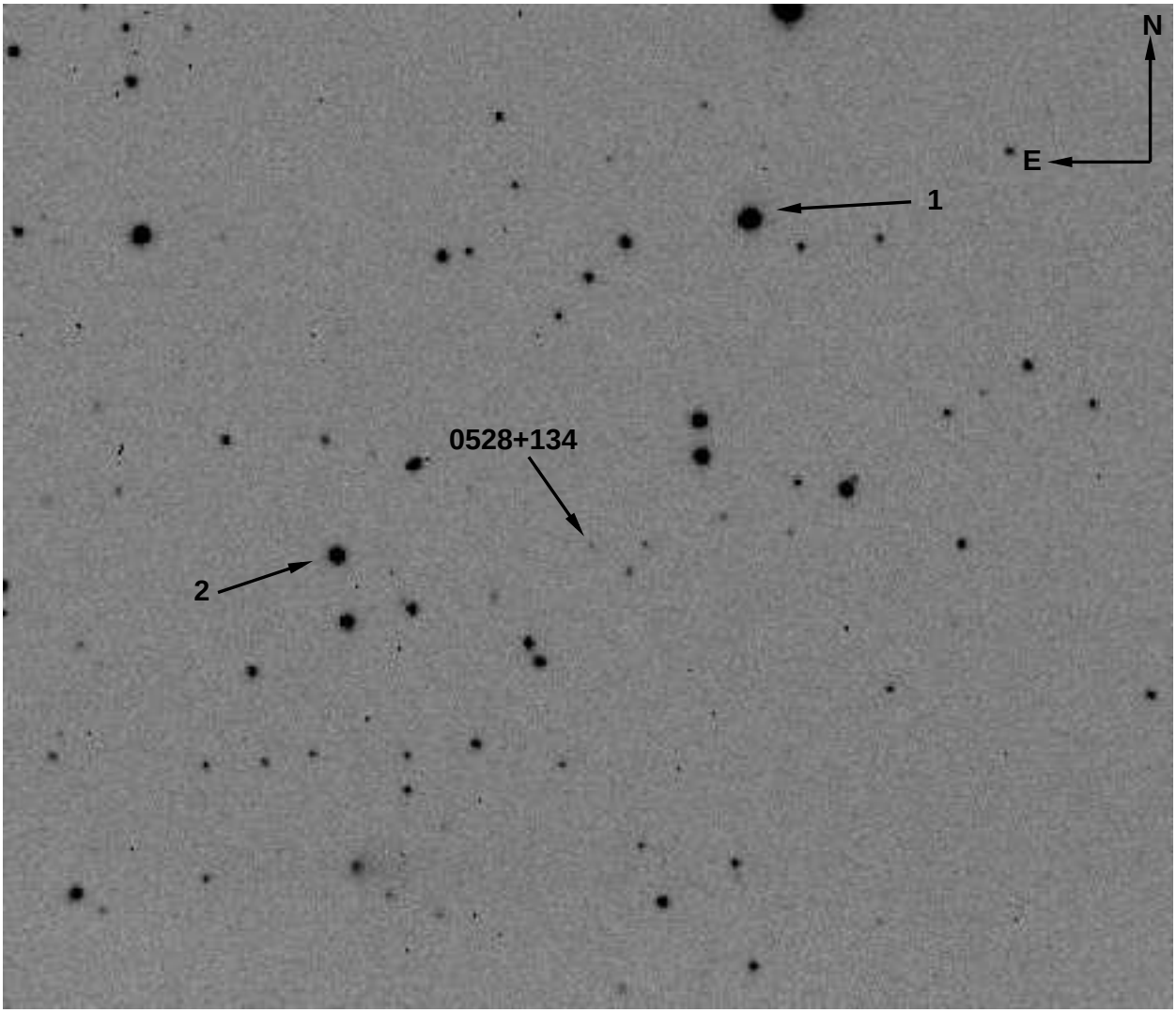

A.3: PKS 0528+134.

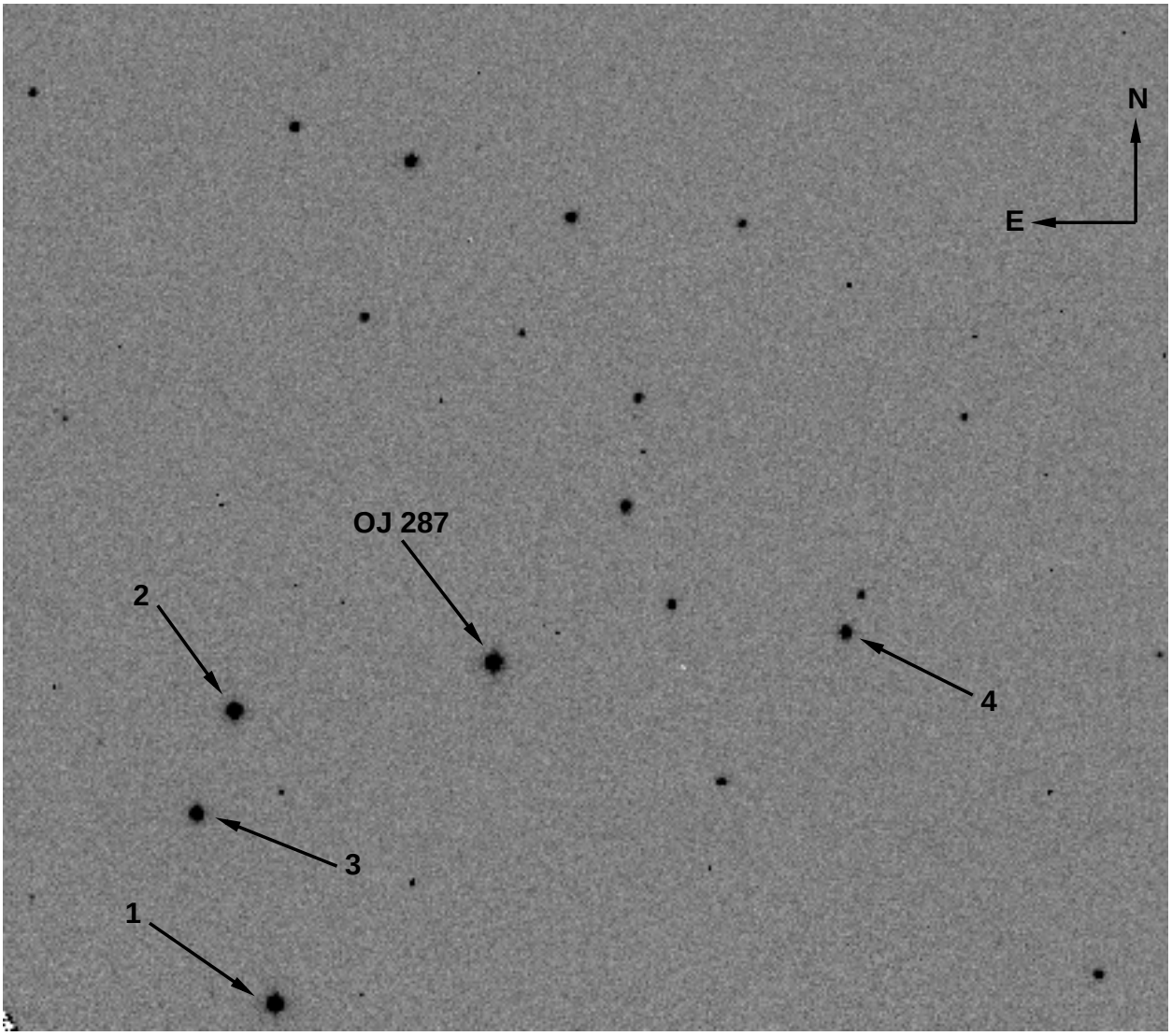

A.4: OJ 287.

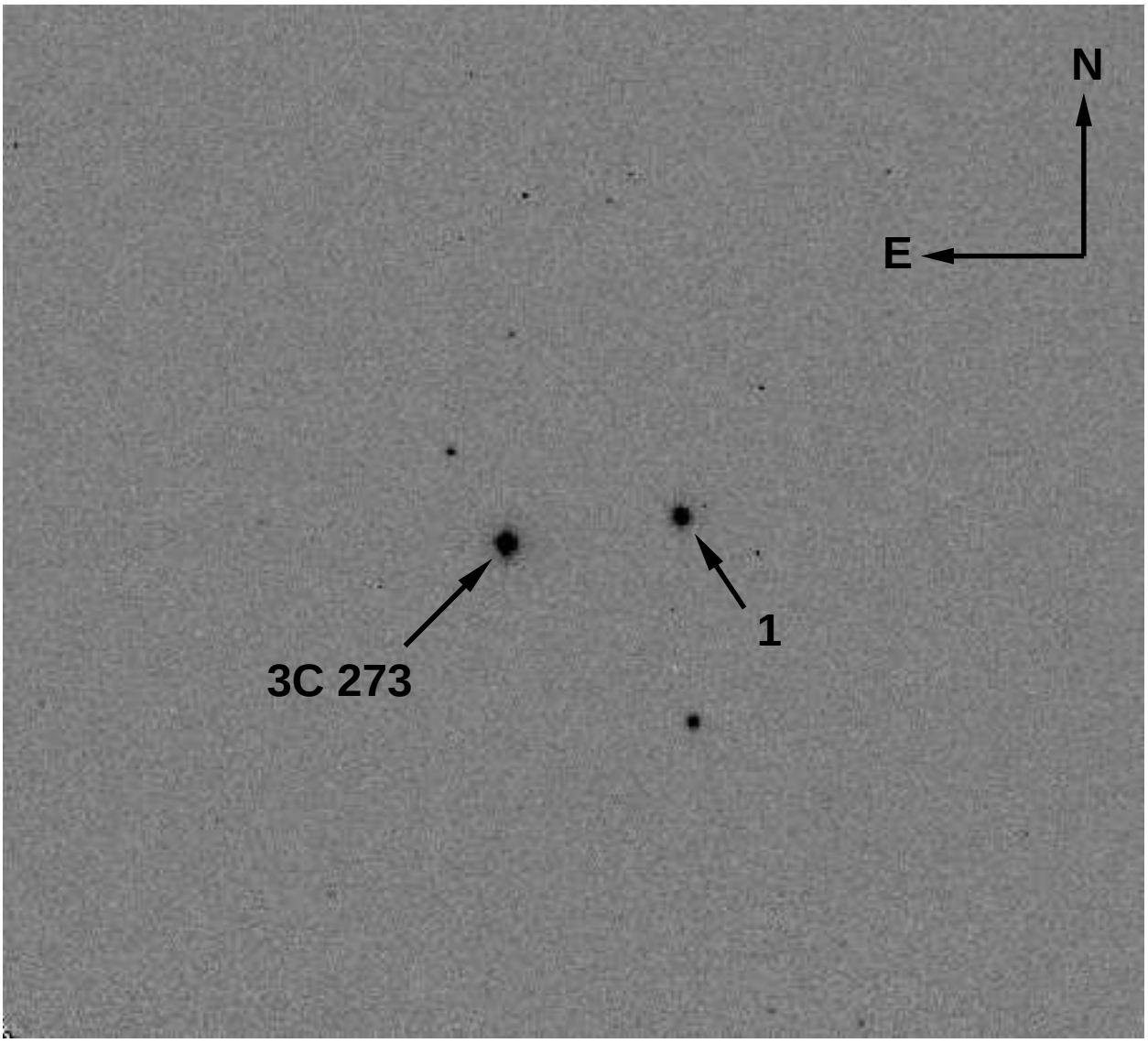

A.5: 3C 273.

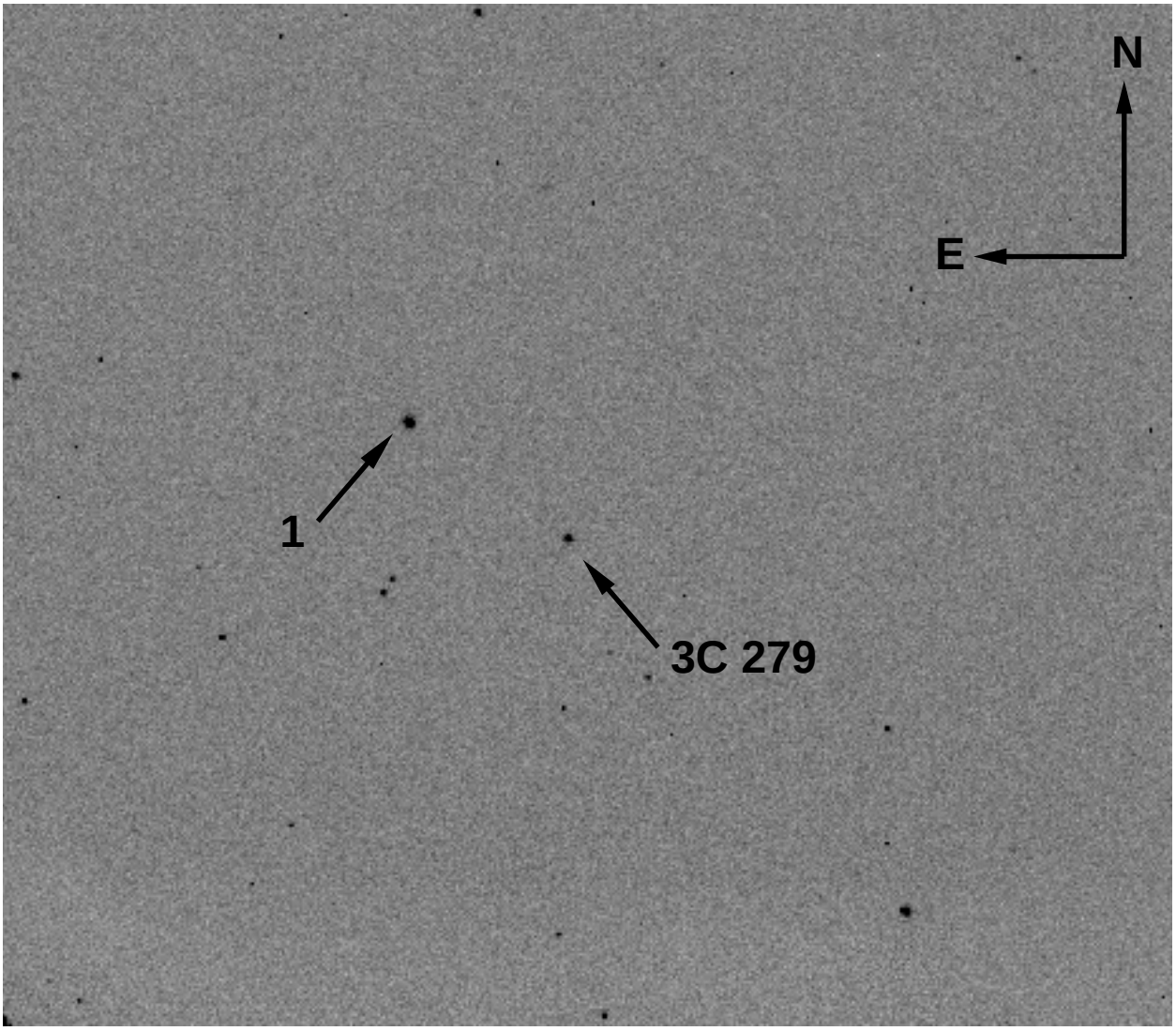

A.6: 3C 279.

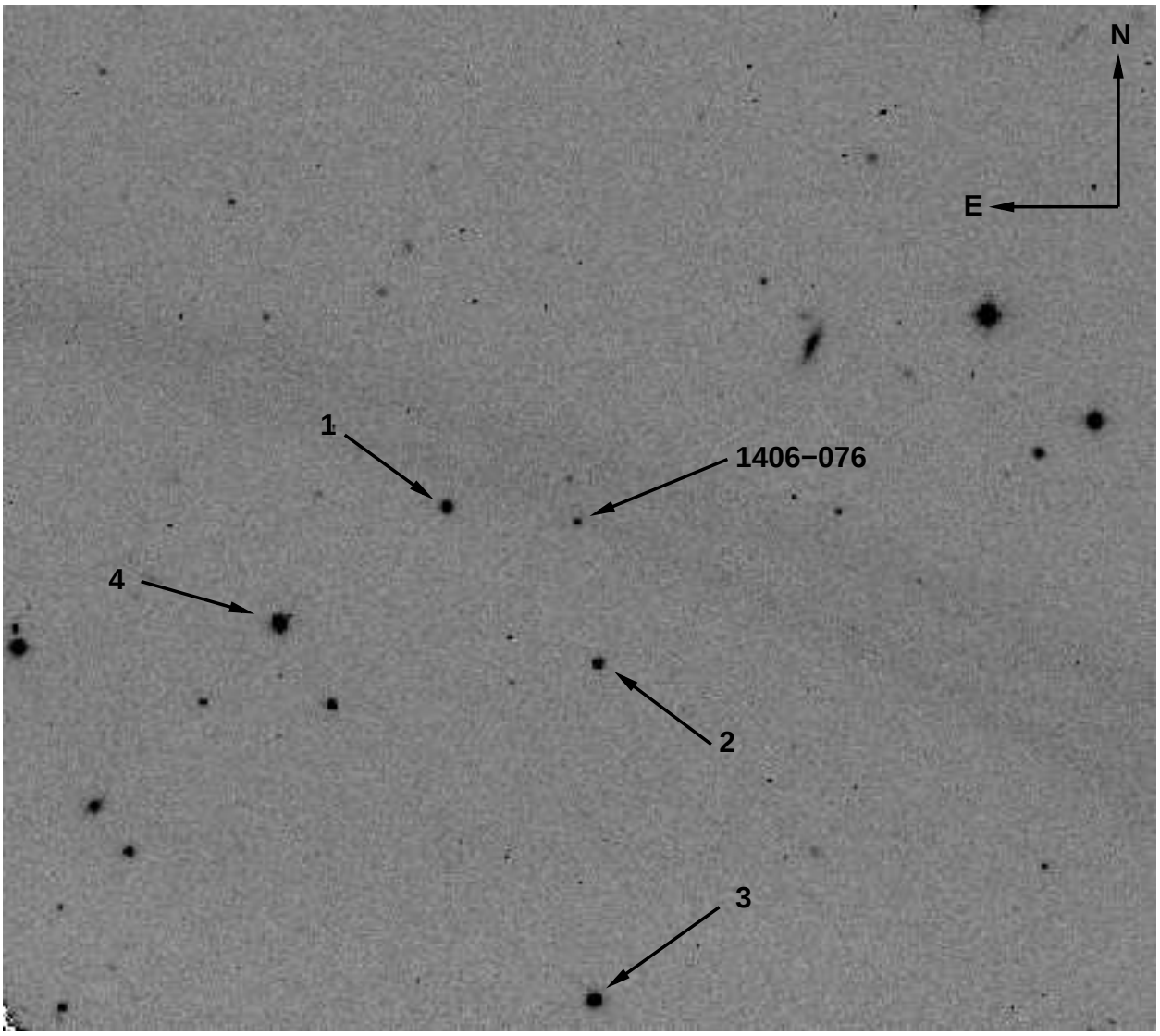

A.7: PKS 1406−076.

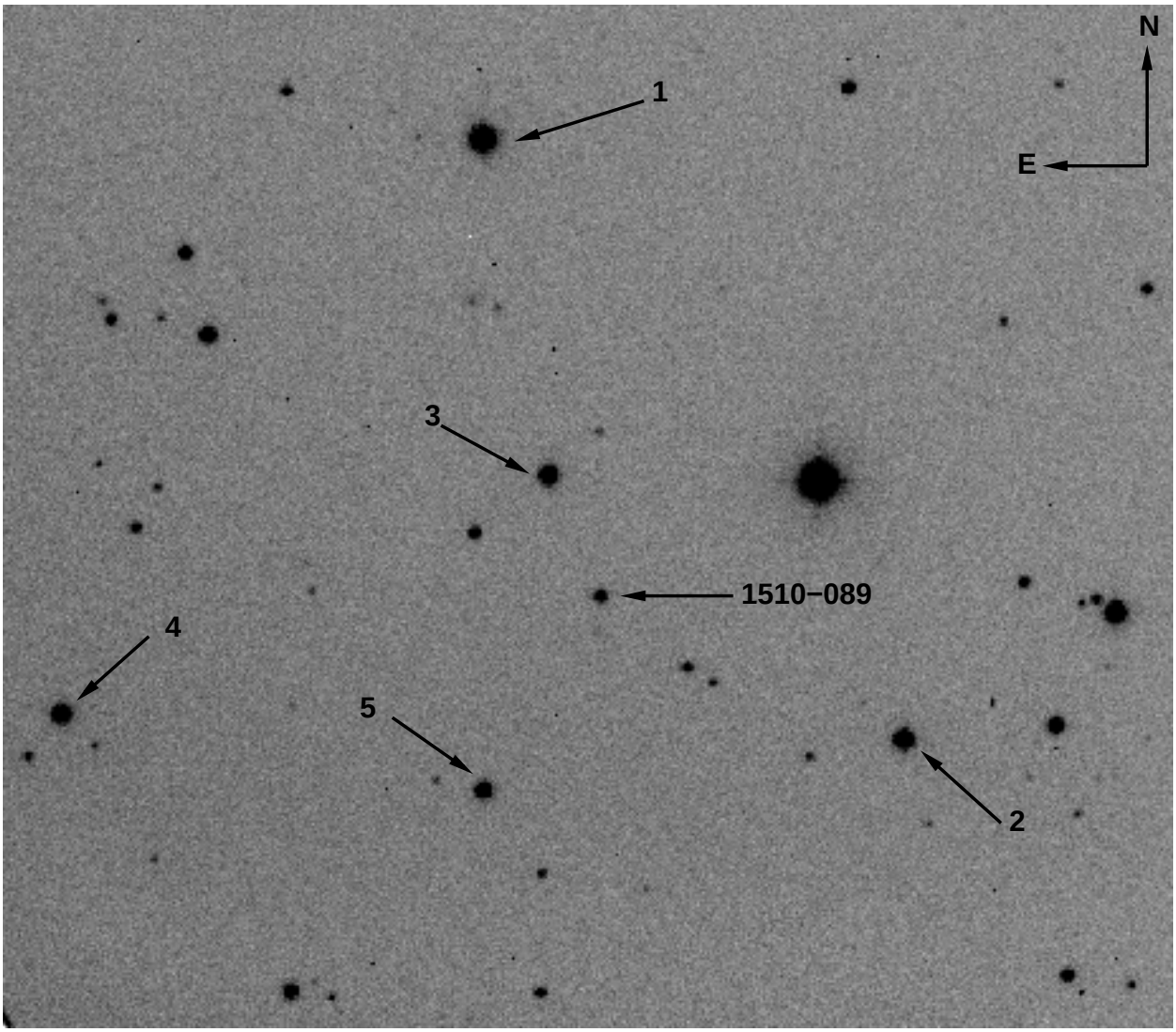

A.8: PKS 1510−089.

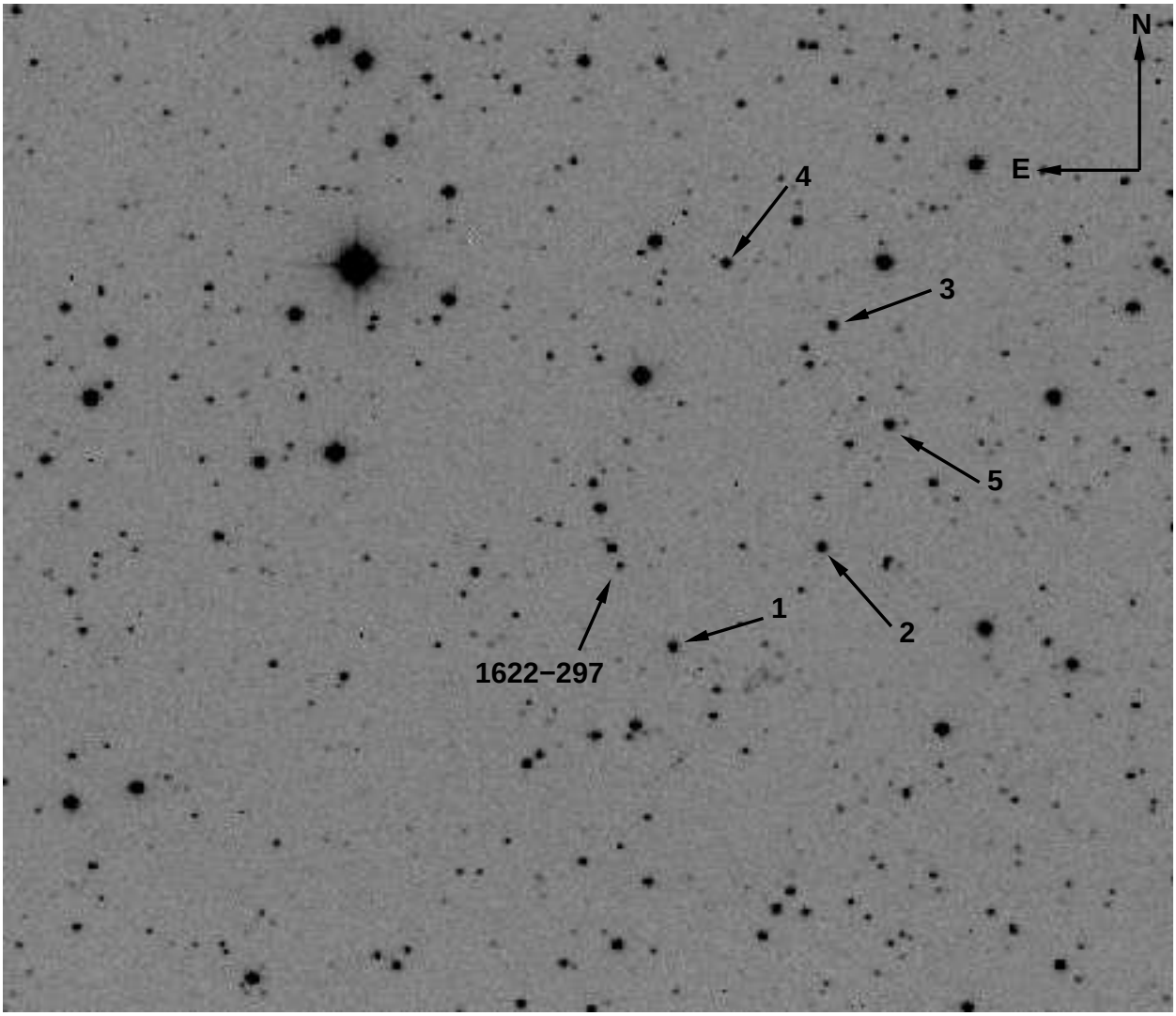

A.9: PKS 1622−297.

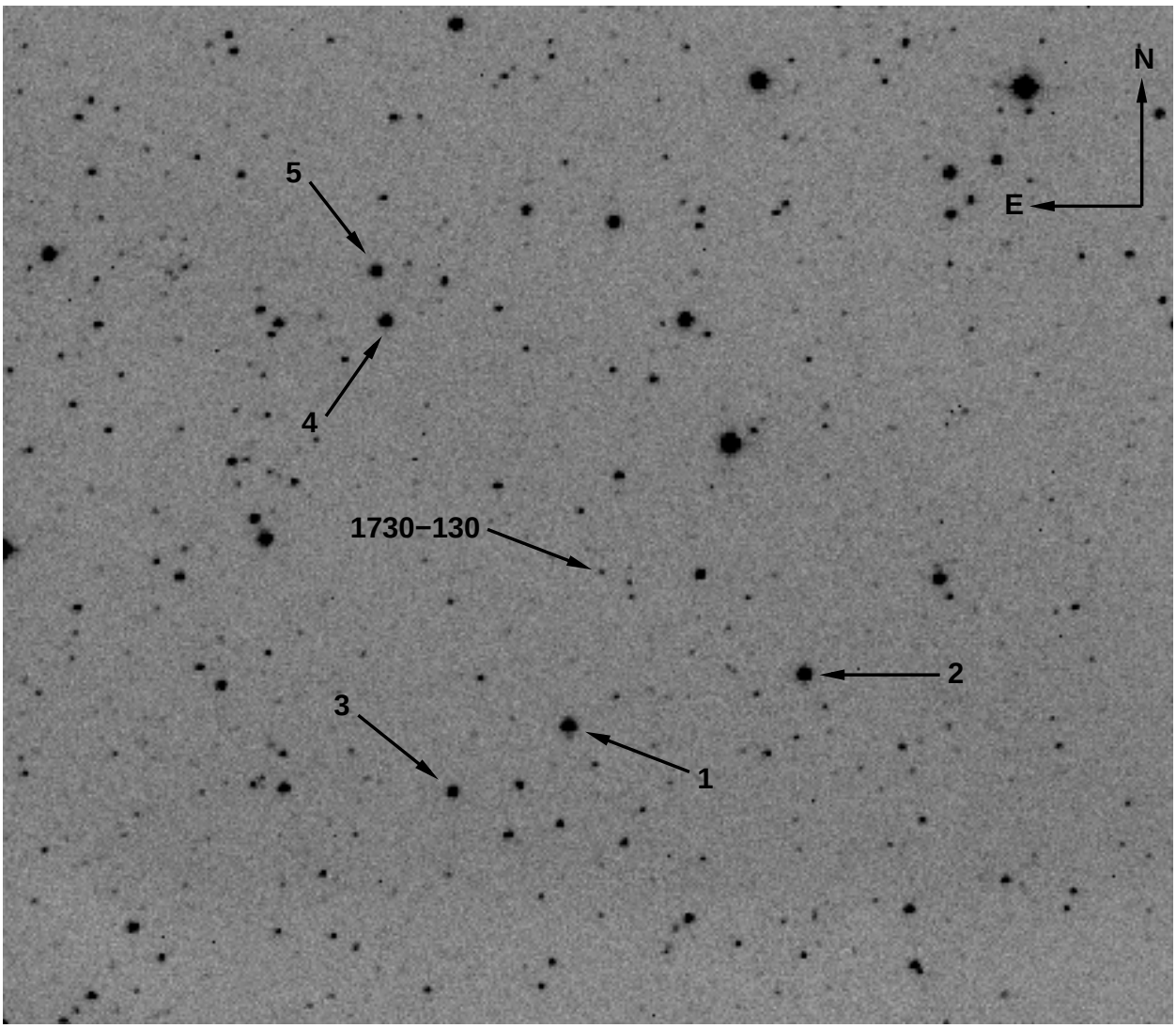

A.10: PKS 1730−130.

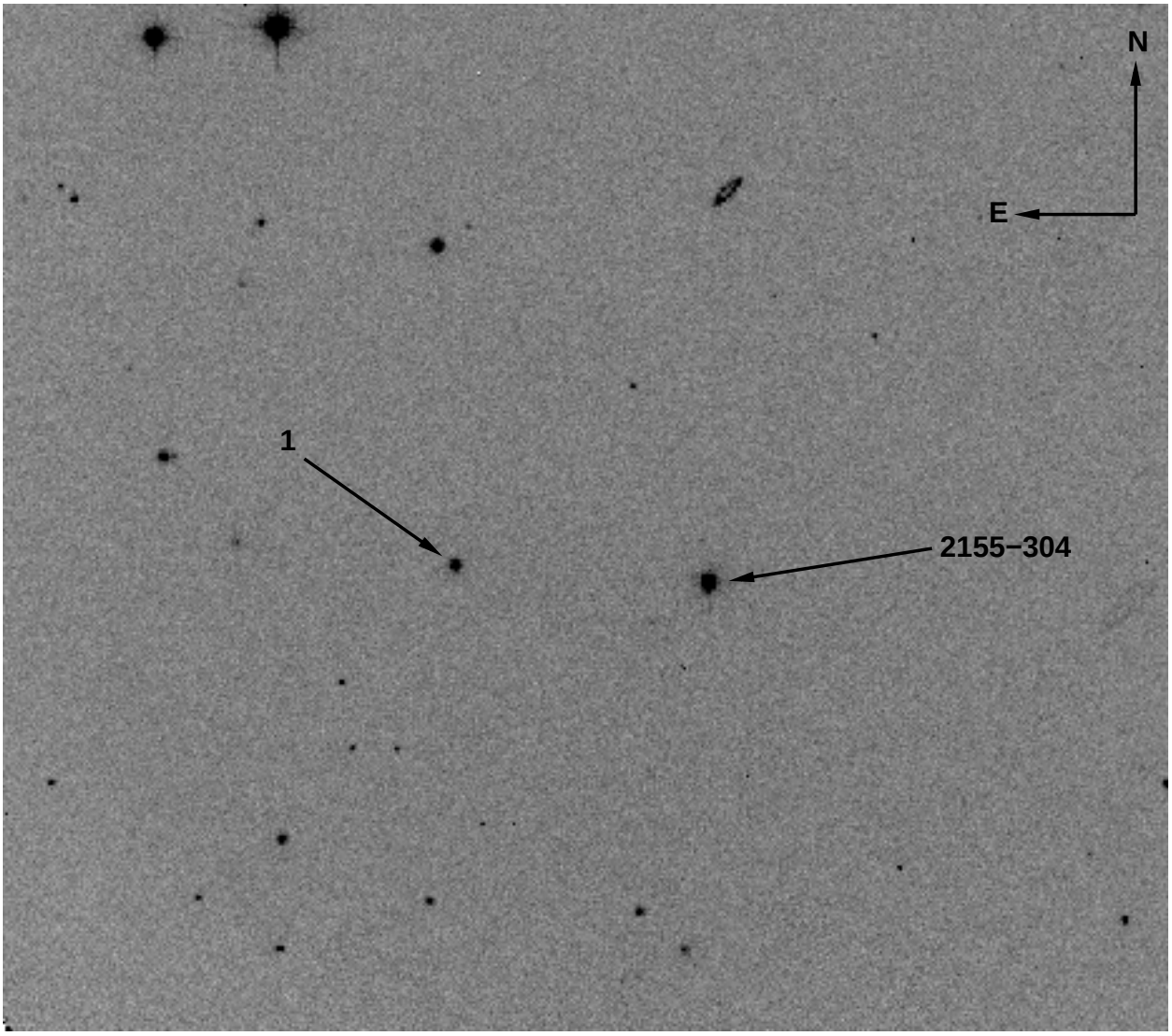

A.11: PKS 2155−304.

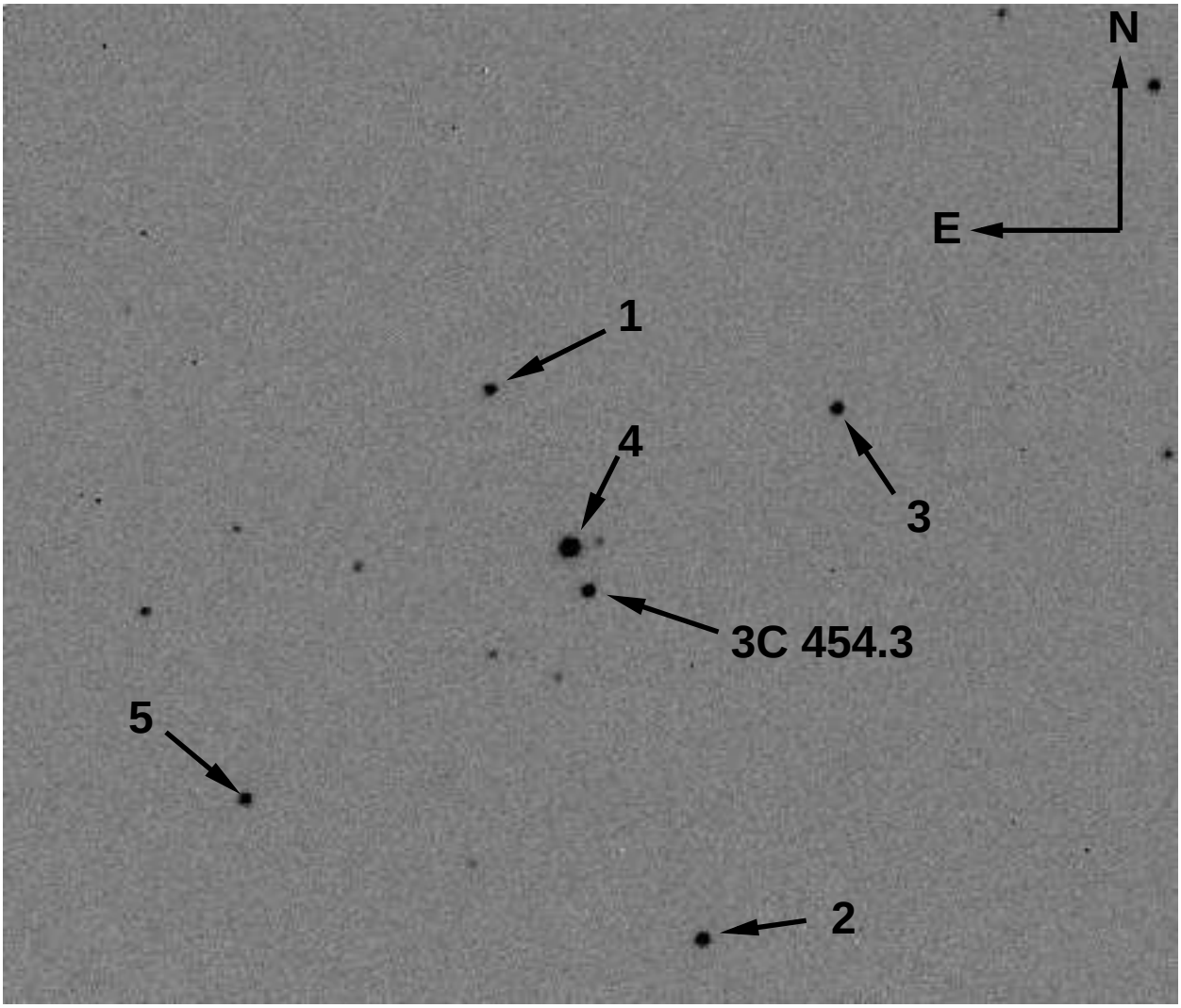

A.12: 3C 454.3.

B. Near-Infrared Finding Charts

We present near-infrared finding charts for each of the 12 SMARTS-monitored blazars discussed in this paper. All figures are J-band. Field of view is approximately $2' \times 2'$. North is to the right of image, East is at the top. Comparison stars are numbered; calibrated magnitudes for our comparison stars are given in Appendix C.

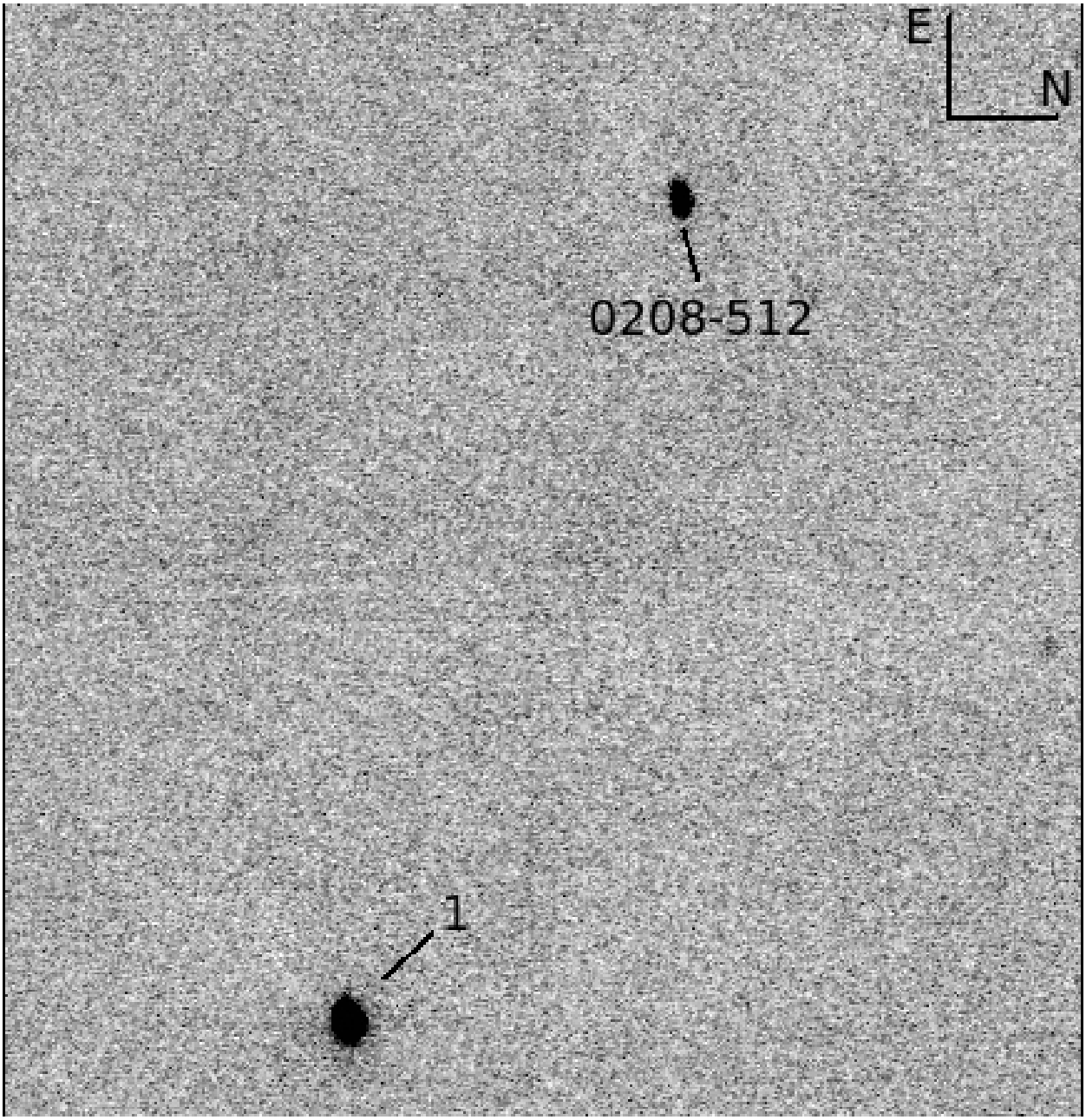

B.1: PKS 0208−512.

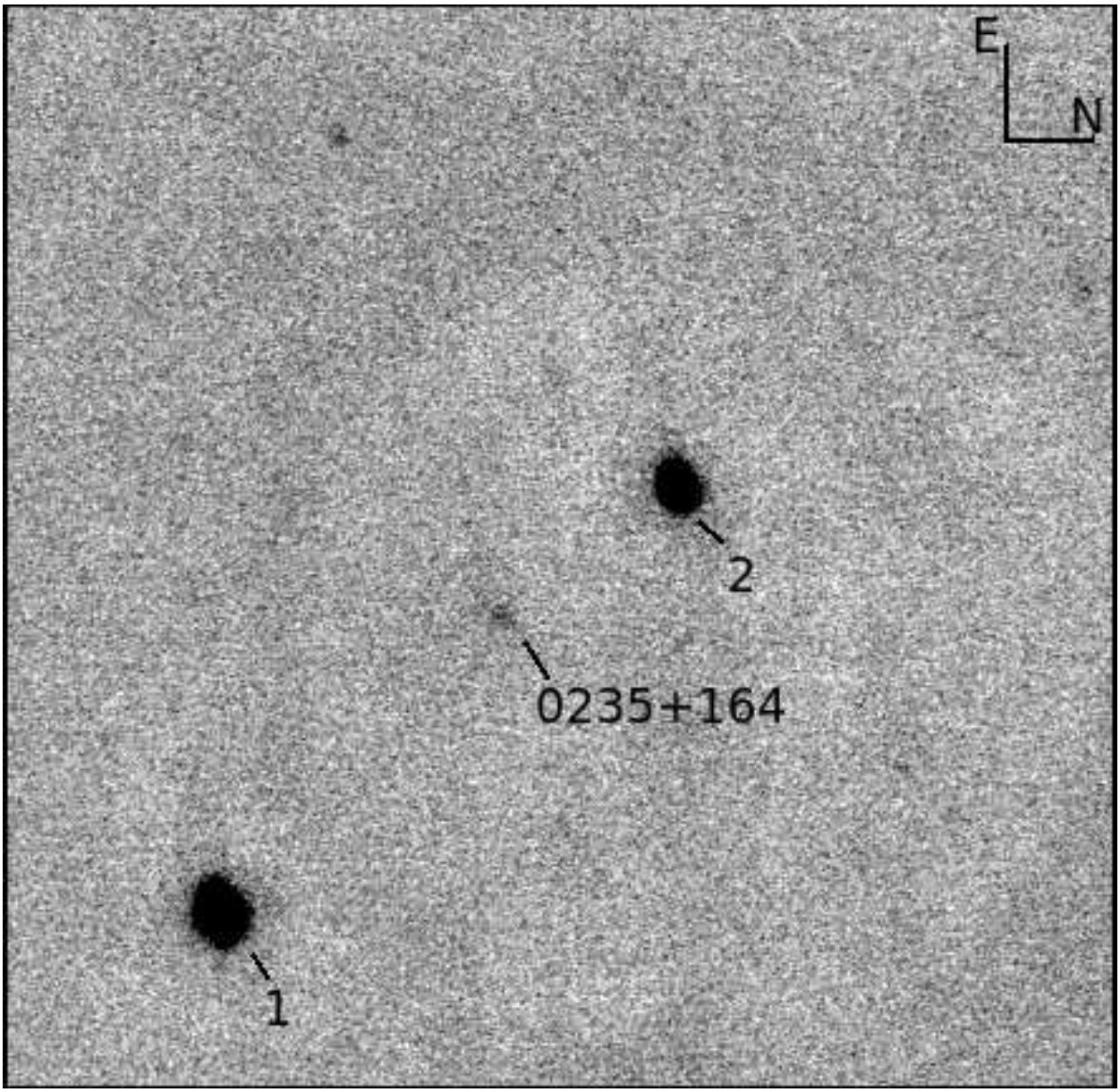

B.2: AO 0235+164.

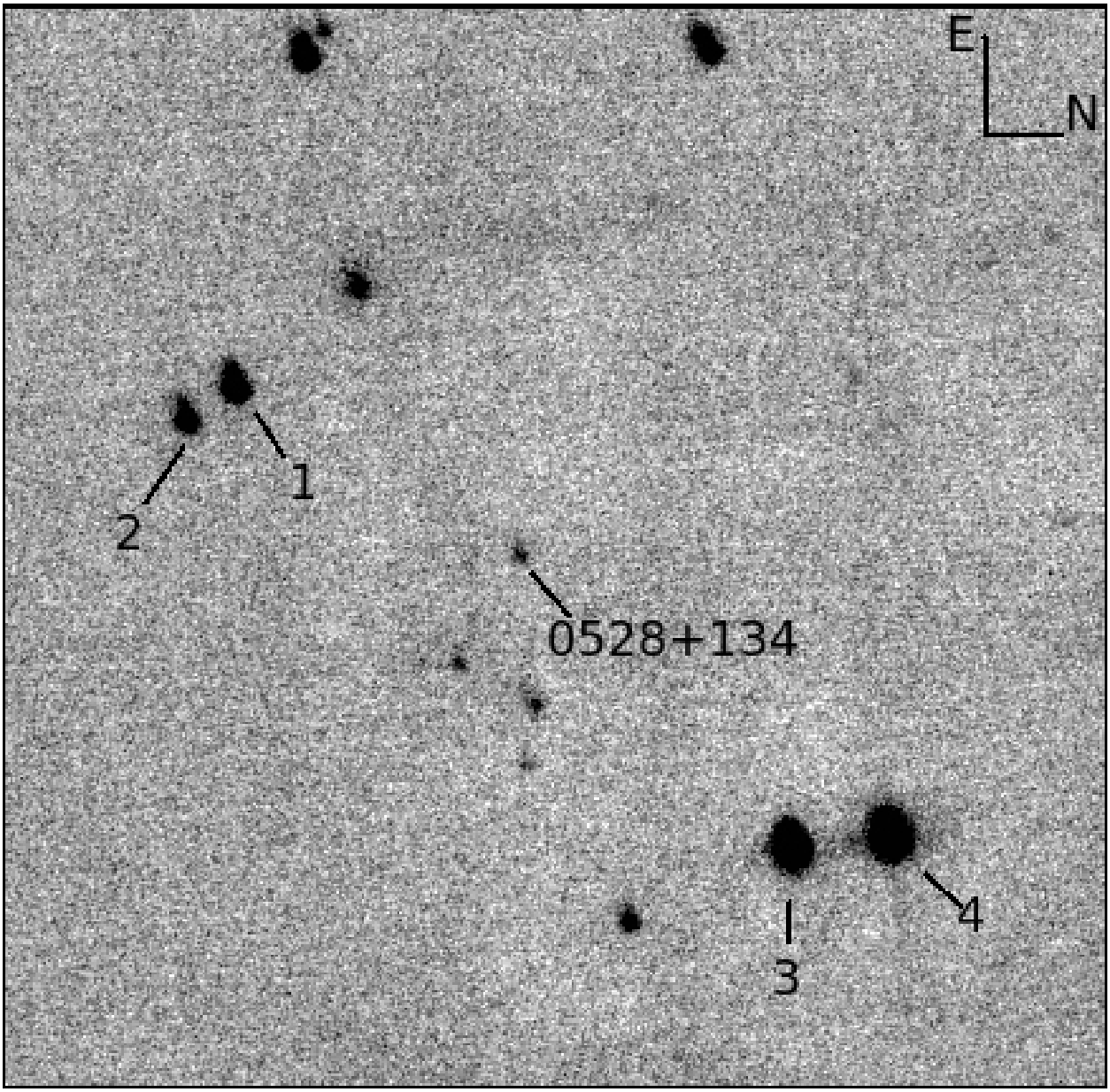

B.3: PKS 0528+134.

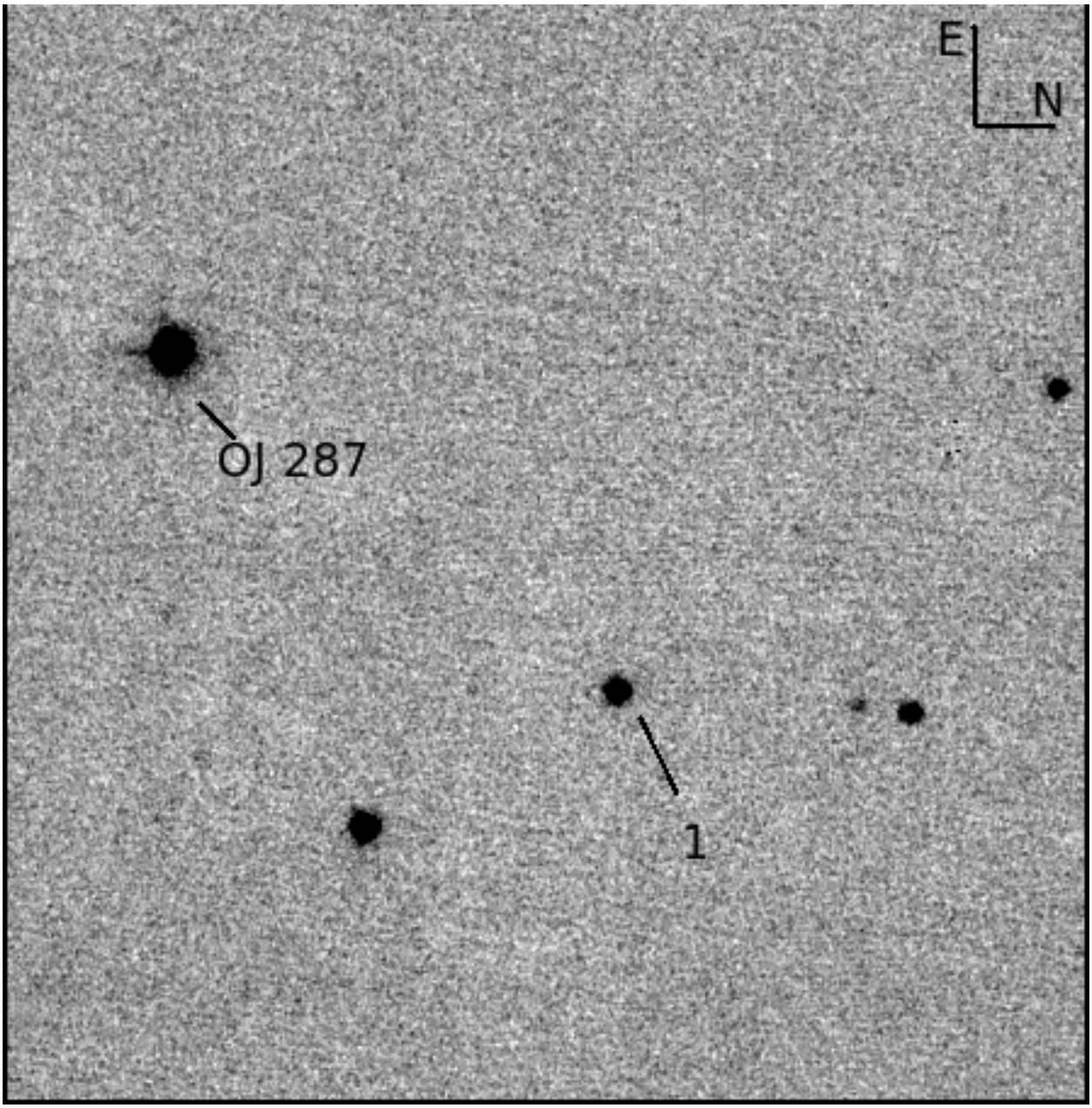

B.4: OJ 287.

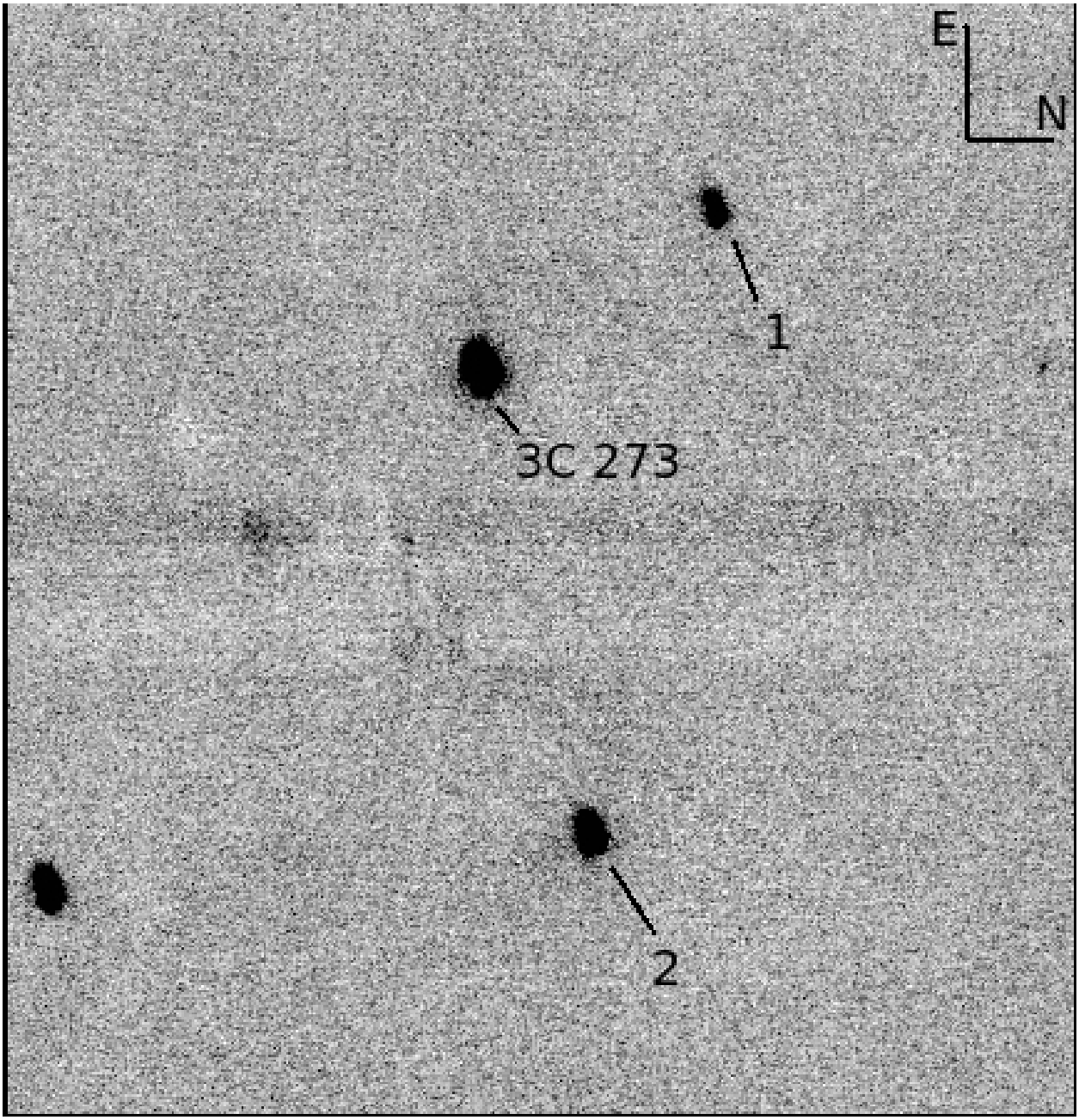

B.5: 3C 273.

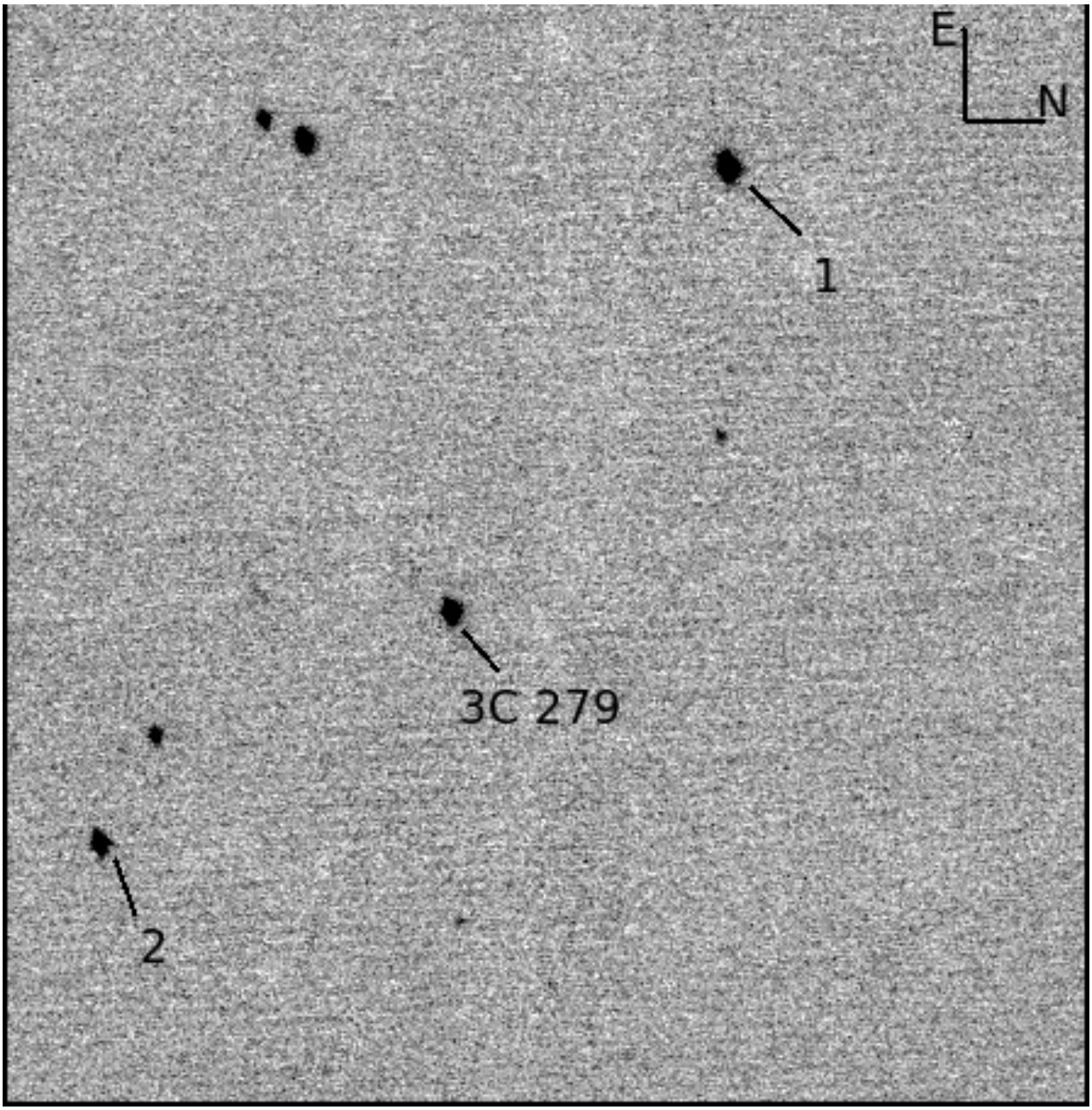

B.6: 3C 279.

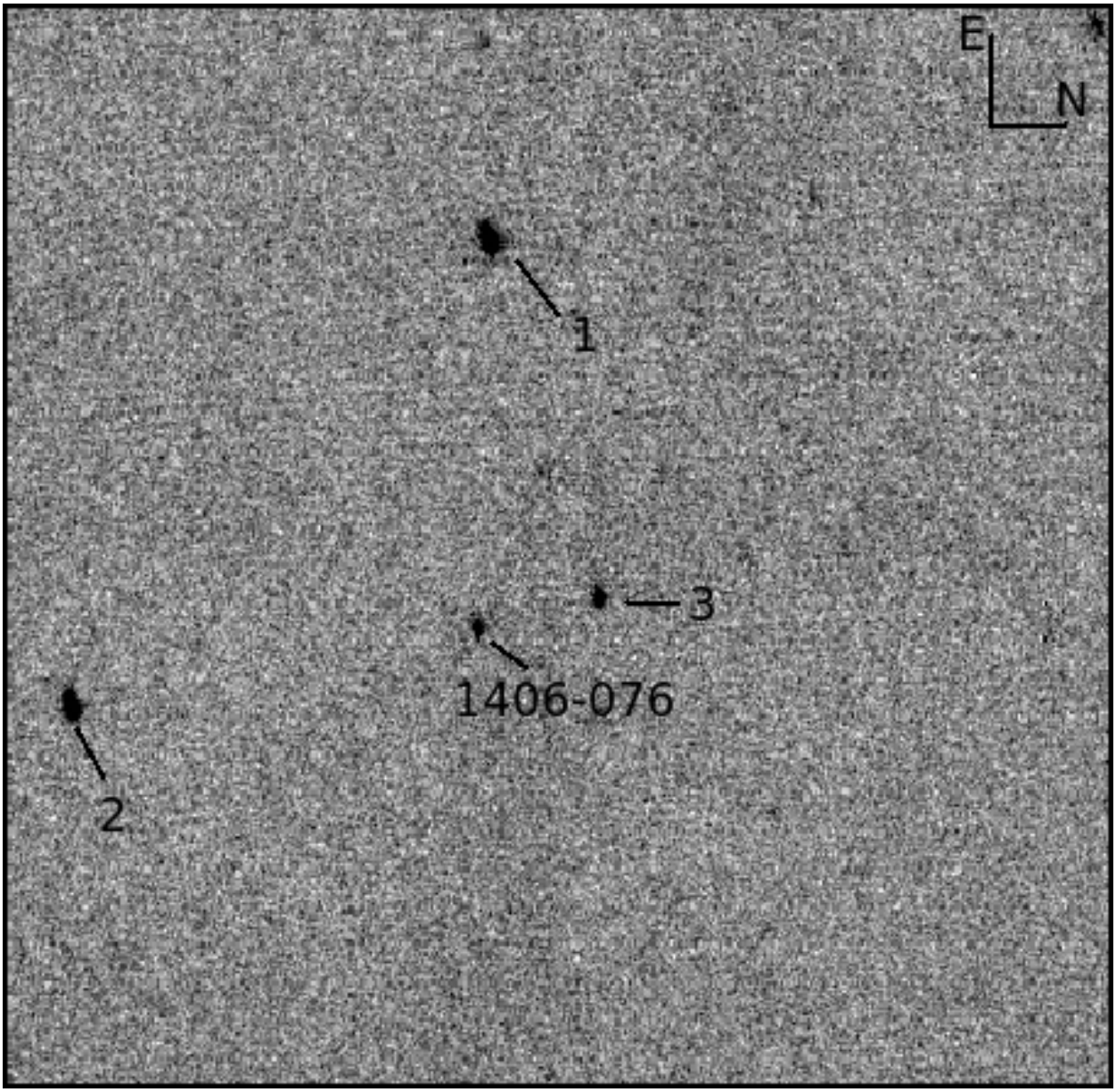

B.7: PKS 1406−076.

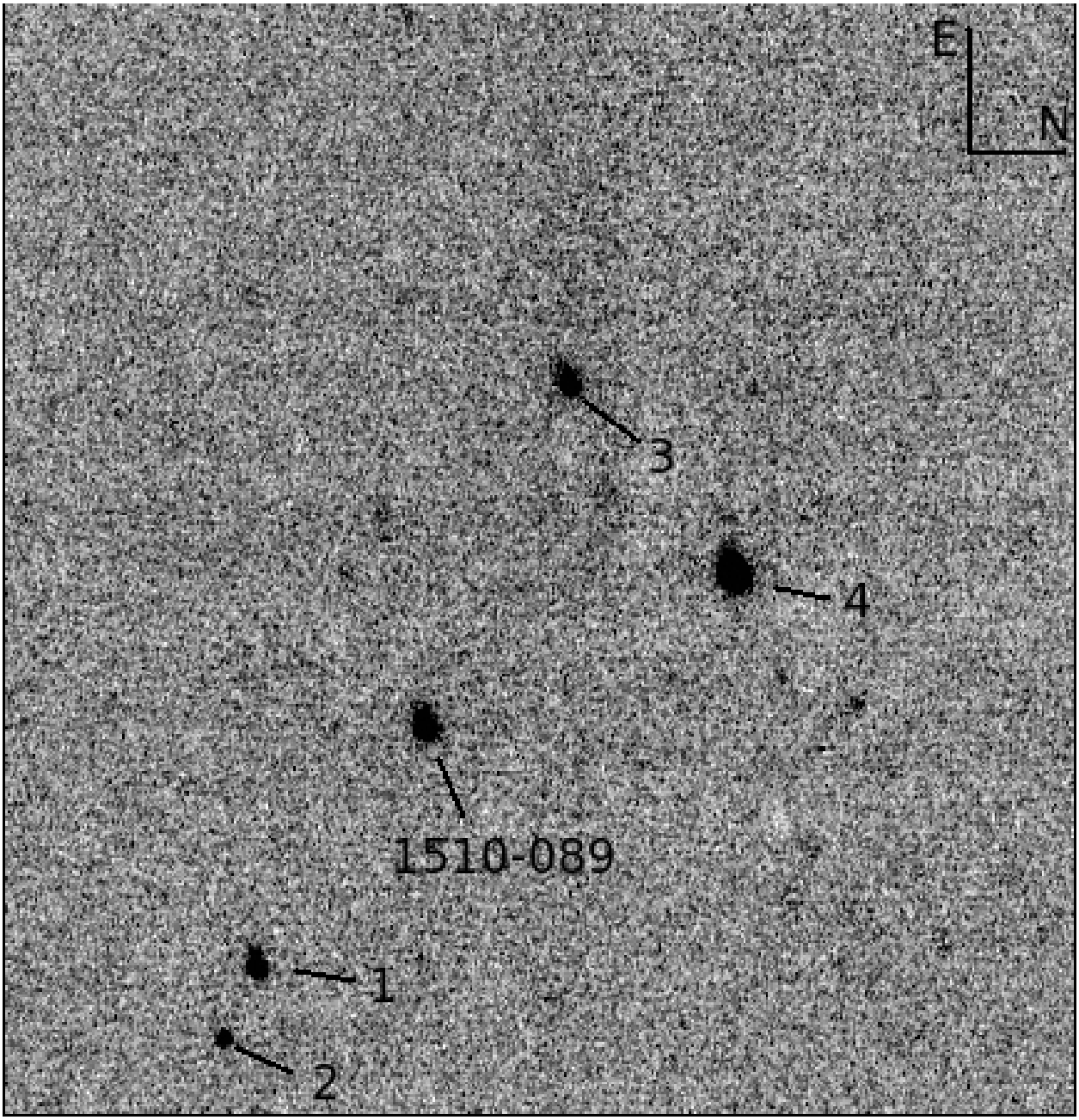

B.8: PKS 1510−089.

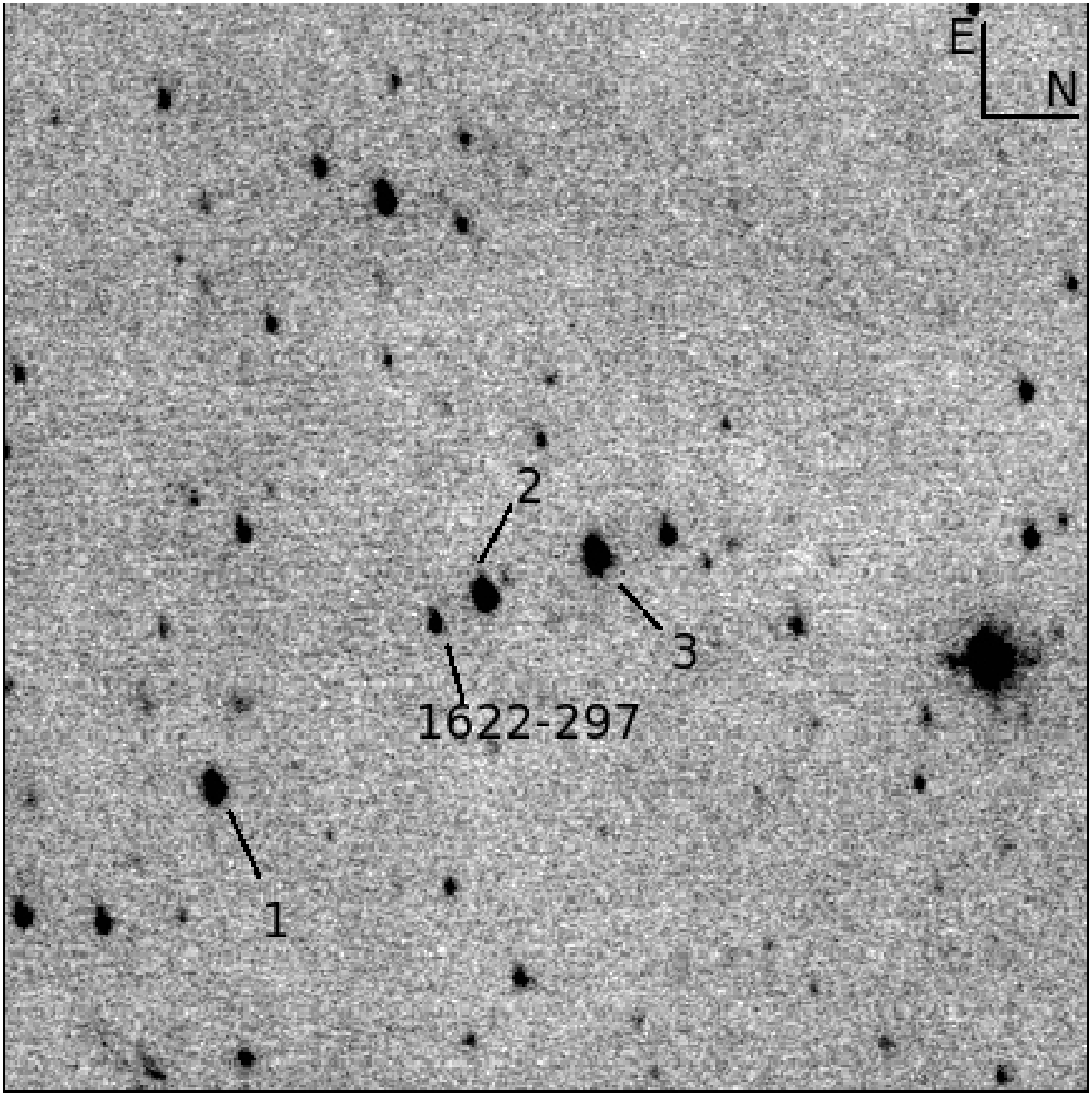

B.9: PKS 1622−297.

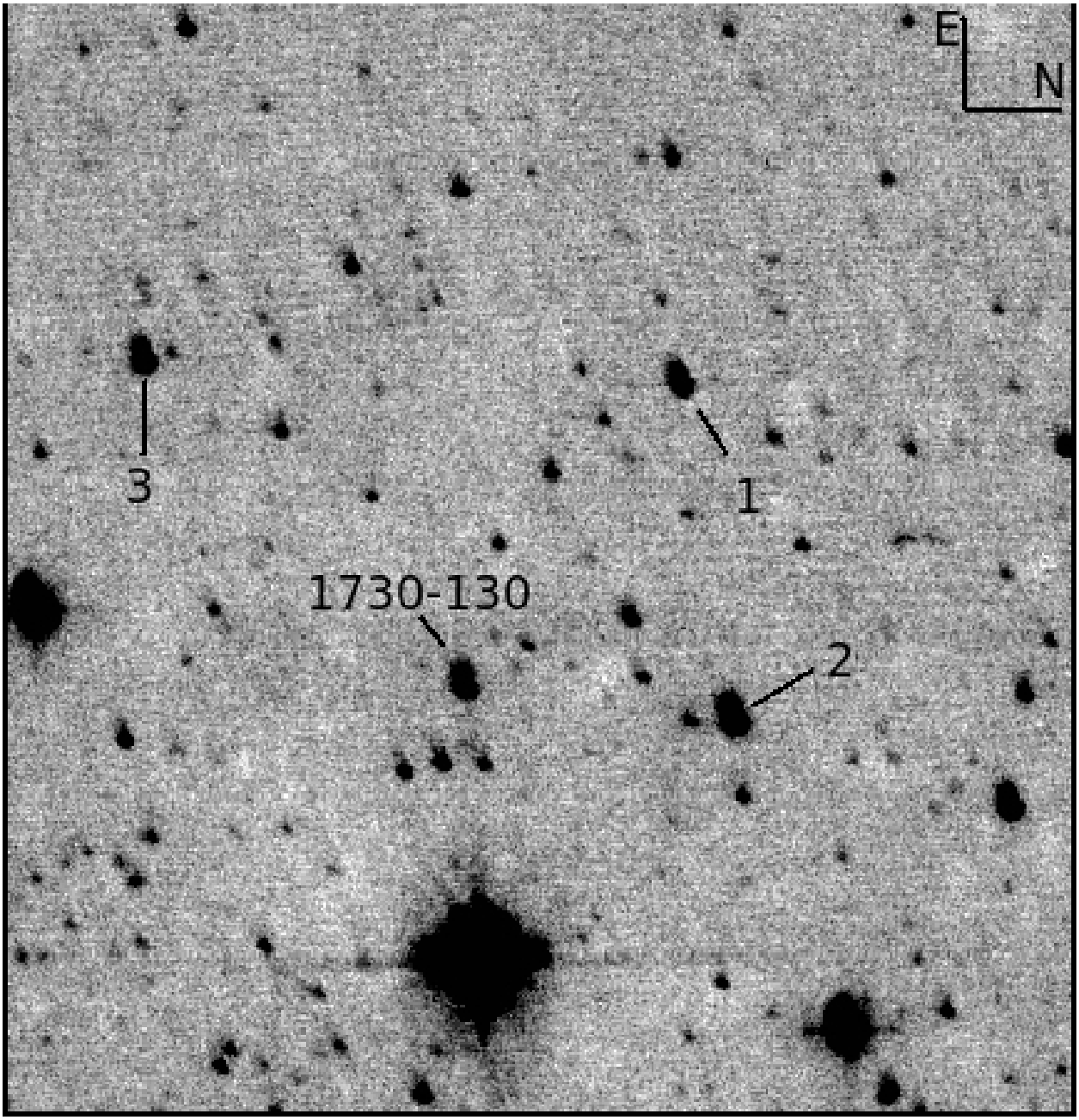

B.10: PKS 1730−130.

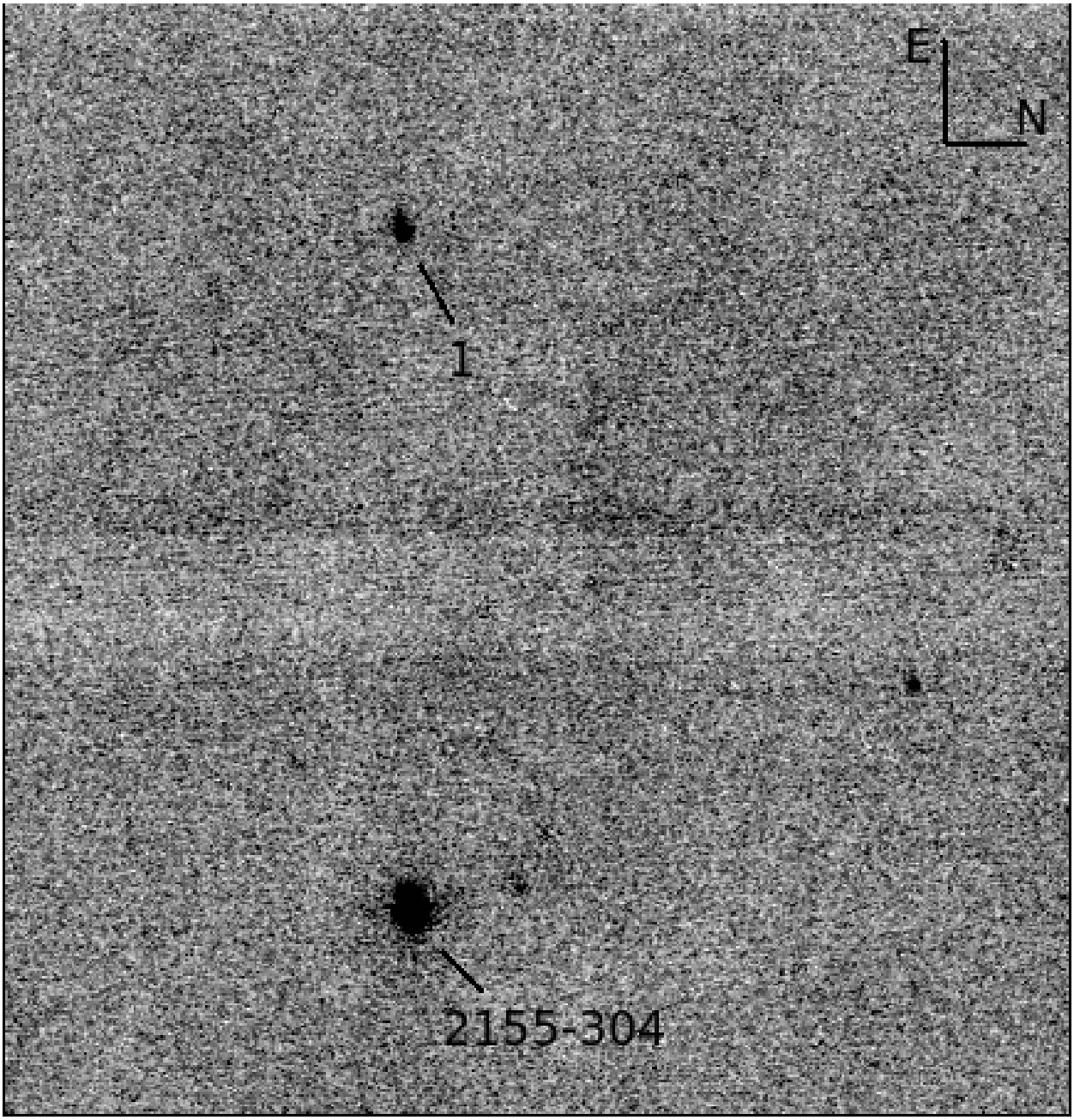

B.11: PKS 2155−304.

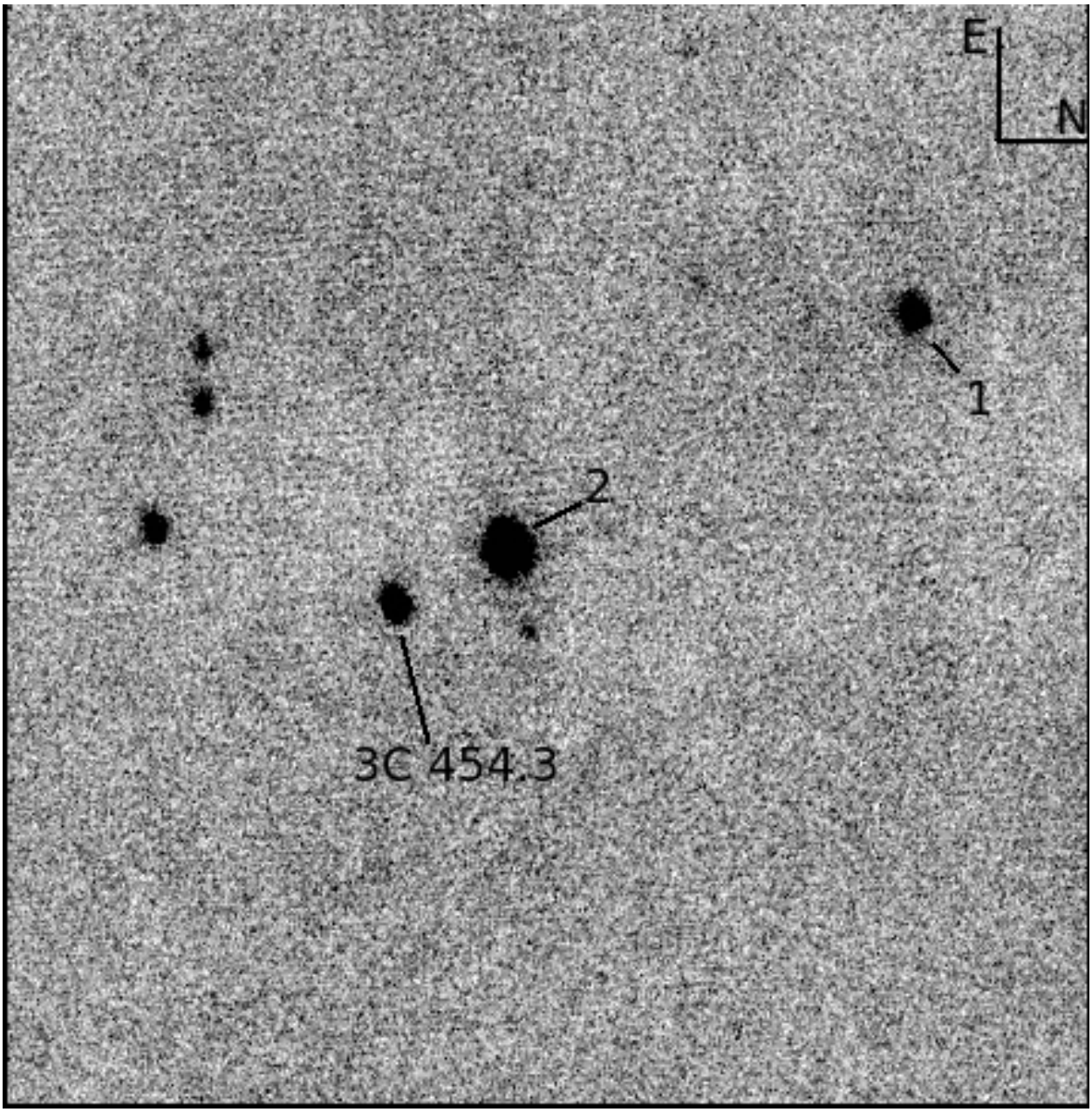

B.12: 3C 454.3.

C. Comparison Star Magnitudes

Calibrated magnitudes for comparison stars indicated in the finding charts presented in Appendixes A and B used as secondary standards for our differential photometry. Comparison stars

The error in calibrating the secondary star magnitudes was found by calculating the 1-σ standard error of the mean over the number of photometric nights on which data for the star were taken. Results that were greater than $\pm$ 3σ from the mean were rejected and the mean and σ were recalculated. This procedure was repeated until no more rejections were made. The resulting 1-σ errors are given in the following tables. Table C.1 gives BVR magnitudes for comparison stars used in optical photometry. Table C.2 gives JK magnitudes for comparison stars used in the infrared photometry.

Table 3: Comparison star optical magnitudes. Errors are 1-σ.

Source	Star	B	V	R
PKS 0208-512	1	16.43 ± 0.03	15.72 ± 0.03	15.27 ± 0.04
	2	16.90 ± 0.04	16.24 ± 0.04	15.79 ± 0.03
	3	15.43 ± 0.04	14.69 ± 0.03	14.29 ± 0.03
AO 0235+164	1	13.61 ± 0.03	13.05 ± 0.03	12.60 ± 0.02
	2	13.55 ± 0.04	12.75 ± 0.03	12.26 ± 0.03
	3	13.72 ± 0.04	12.98 ± 0.03	12.55 ± 0.03
	4	14.70 ± 0.04	14.05 ± 0.03	13.64 ± 0.03
	5	15.74 ± 0.03	14.80 ± 0.03	14.22 ± 0.03
PKS 0528+134	1	15.90 ± 0.05	14.79 ± 0.03	13.99 ± 0.05
	2	16.81 ± 0.03	15.80 ± 0.03	15.09 ± 0.03
OJ 287	1	15.03 ± 0.05	14.25 ± 0.04	13.69 ± 0.05
	2	15.18 ± 0.04	14.65 ± 0.04	14.26 ± 0.04
	3	15.53 ± 0.05	14.97 ± 0.04	14.55 ± 0.04
	4	16.67 ± 0.05	15.94 ± 0.04	15.43 ± 0.04
3C 273	1	14.14 ± 0.04	13.53 ± 0.04	13.14 ± 0.03
3C 279	1	16.76 ± 0.04	15.92 ± 0.03	15.35 ± 0.03
PKS 1406-076	1	17.67 ± 0.05	16.89 ± 0.03	16.31 ± 0.03
	2	17.96 ± 0.05	17.23 ± 0.04	16.71 ± 0.03
	3	16.55 ± 0.05	15.74 ± 0.03	15.22 ± 0.03
	4	16.04 ± 0.04	15.40 ± 0.05	14.96 ± 0.03
PKS 1510-089	1	13.82 ± 0.04	13.29 ± 0.03	12.96 ± 0.02
	2	15.16 ± 0.05	14.44 ± 0.03	13.98 ± 0.03
	3	15.32 ± 0.04	14.66 ± 0.03	14.24 ± 0.03
	4	15.55 ± 0.04	14.82 ± 0.03	14.36 ± 0.03
	5	16.18 ± 0.04	15.23 ± 0.03	14.59 ± 0.02
PKS 1622-297	1	17.79 ± 0.06	16.66 ± 0.05	16.00 ± 0.03
	2	17.83 ± 0.06	16.68 ± 0.05	15.89 ± 0.05
	3	18.21 ± 0.06	17.06 ± 0.05	16.24 ± 0.04
	4	18.16 ± 0.06	17.04 ± 0.04	16.20 ± 0.03
	5	17.41 ± 0.05	16.59 ± 0.05	16.04 ± 0.03
PKS 1730-130	1	16.11 ± 0.04	14.50 ± 0.03	13.46 ± 0.03
	2	15.71 ± 0.05	14.28 ± 0.03	13.37 ± 0.03
	3	16.83 ± 0.05	15.36 ± 0.03	14.41 ± 0.03
	4	15.76 ± 0.05	14.68 ± 0.03	13.98 ± 0.03
	5	16.60 ± 0.05	15.05 ± 0.04	14.04 ± 0.02
PKS 2155-304	1	15.97 ± 0.03	15.33 ± 0.04	14.94 ± 0.03
3C 454.3	1	16.76 ± 0.05	15.87 ± 0.04	15.29 ± 0.04
	2	15.82 ± 0.05	15.17 ± 0.05	14.74 ± 0.03
	3	16.89 ± 0.05	15.71 ± 0.05	14.92 ± 0.03
	4	14.57 ± 0.05	13.65 ± 0.04	13.09 ± 0.03
	5	16.65 ± 0.05	15.77 ± 0.04	15.20 ± 0.04

Table 4: Comparison star near-infrared magnitudes. Errors are 1-σ.

Source	Star	J	K
PKS 0208-512	1	12.16 ± 0.04	11.81 ± 0.07
AO 0235+164	1	11.96 ± 0.04	11.68 ± 0.06
	2	12.97 ± 0.04	12.14 ± 0.09
PKS 0528+134	1	14.03 ± 0.08	
	2	12.72 ± 0.06	
	3	12.32 ± 0.05	
OJ 287	1	14.58 ± 0.080	13.79 ± 0.10
3C 273	1	13.64 ± 0.06	
	2	12.29 ± 0.05	
3C 279	1	14.41 ± 0.07	13.86 ± 0.12
	2	15.47 ± 0.14	13.94 ± 0.20
PKS 1406-076	1	15.32 ± 0.07	14.84 ± 0.16
	2	15.77 ± 0.11	15.30 ± 0.47
PKS 1510-089	1	15.61 ± 0.13	14.71 ± 0.27
	2	15.57 ± 0.11	14.44 ± 0.32
	3	13.49 ± 0.05	12.77 ± 0.12
PKS 1622-297	1	14.43 ± 0.11	13.47 ± 0.14
	2	13.83 ± 0.11	12.69 ± 0.12
	3	13.53 ± 0.08	12.67 ± 0.11
PKS 1730-130	1	14.37 ± 0.07	13.17 ± 0.10
	2	13.06 ± 0.07	11.96 ± 0.06
	3	14.60 ± 0.07	13.48 ± 0.10
PKS 2155-304	1	14.30 ± 0.06	13.72 ± 0.14
3C 454.3	1	14.26 ± 0.10	13.49 ± 0.15
	2	11.88 ± 0.07	11.31 ± 0.61

REFERENCES

Abdo, A. A., Ackermann, M., Ajello, M., Axelsson, M., Baldini, L., Ballet, J., Barbiellini, G., Bastieri, D., Baughman, B. M., Bechtol, K., & et al. 2010, Nature, 463, 919

Agudo, I., Marscher, A. P., Jorstad, S. G., Larionov, V. M., Gómez, J. L., Lähteenmäki, A., Smith, P. S., Nilsson, K., Readhead, A. C. S., Aller, M. F., Heidt, J., Gurwell, M., Thum, C., Wehrle, A. E., Nikolashvili, M. G., Aller, H. D., Benítez, E., Blinov,

D. A., Hagen-Thorn, V. A., Hiriart, D., Jannuzi, B. T., Joshi, M., Kimeridze, G. N., Kurtanidze, O. M., Kurtanidze, S. O., Lindfors, E., Molina, S. N., Morozova, D. A., Nieppola, E., Olmstead, A. R., Reinthal, R., Roca-Sogorb, M., Schmidt, G. D., Sigua, L. A., Sillanpää, A., Takalo, L., Taylor, B., Tornikoski, M., Troitsky, I. S., Zook, A. C., & Wiesemeyer, H. 2011, ApJ, 735, L10+

Alcock, C., Allsman, R. A., Alves, D. R., Axelrod, T. S., Becker, A. C., Bennett, D. P., Cook, K. H., Dalal, N., Drake, A. J., Freeman, K. C., Geha, M., Griest, K., Lehner, M. J., Marshall, S. L., Minniti, D., Nelson, C. A., Peterson, B. A., Popowski, P., Pratt, M. R., Quinn, P. J., Stubbs, C. W., Sutherland, W., Tomaney, A. B., Vandehei, T., & Welch, D. 2000, ApJ, 542, 281

Bonning, E. W., Bailyn, C., Urry, C. M., Buxton, M., Fossati, G., Maraschi, L., Coppi, P., Scalzo, R., Isler, J., & Kaptur, A. 2009, ApJ, 697, L81

Böttcher, M. 2007, Ap&SS, 309, 95

Coppi, P. S. 1992, MNRAS, 258, 657

DePoy, D. L., Atwood, B., Belville, S. R., Brewer, D. F., Byard, P. L., Gould, A., Mason, J. A., O'Brien, T. P., Pappalardo, D. P., Pogge, R. W., Steinbrecher, D. P., & Teiga, E. J. 2003, in Society of Photo-Optical Instrumentation Engineers (SPIE) Conference Series, Vol. 4841, Society of Photo-Optical Instrumentation Engineers (SPIE) Conference Series, ed. M. Iye & A. F. M. Moorwood, 827–838

Dermer, C. D. & Schlickeiser, R. 1993, ApJ, 416, 458

Edelson, R., Turner, T. J., Pounds, K., Vaughan, S., Markowitz, A., Marshall, H., Dobbie, P., & Warwick, R. 2002, ApJ, 568, 610

Edelson, R. A. & Krolik, J. H. 1988, ApJ, 333, 646

Fossati, G., Maraschi, L., Celotti, A., Comastri, A., & Ghisellini, G. 1998, MNRAS, 299, 433

Ghisellini, G. & Celotti, A. 2001, MNRAS, 327, 739

Ghisellini, G. & Madau, P. 1996, MNRAS, 280, 67

Ghisellini, G. & Tavecchio, F. 2010, MNRAS, 409, L79

Jones, T. W., O'dell, S. L., & Stein, W. A. 1974, ApJ, 188, 353

Kataoka, J., Takahashi, T., Makino, F., Inoue, S., Madejski, G. M., Tashiro, M., Urry, C. M., & Kubo, H. 2000, ApJ, 528, 243

Konigl, A. 1981, ApJ, 243, 700

Landolt, A. U. 1992, AJ, 104, 340

Maccarone, T. J. & Coppi, P. S. 2003, MNRAS, 338, 189

Malkan, M. A. 1983, ApJ, 268, 582

Marscher, A. P., Jorstad, S. G., Larionov, V. M., Aller, M. F., Aller, H. D., Lähteenmäki, A., Agudo, I., Smith, P. S., Gurwell, M., Hagen-Thorn, V. A., Konstantinova, T. S., Larionova, E. G., Larionova, L. V., Melnichuk, D. A., Blinov, D. A., Kopatskaya, E. N., Troitsky, I. S., Tornikoski, M., Hovatta, T., Schmidt, G. D., D'Arcangelo, F. D., Bhattarai, D., Taylor, B., Olmstead, A. R., Manne-Nicholas, E., Roca-Sogorb, M., Gómez, J. L., McHardy, I. M., Kurtanidze, O., Nikolashvili, M. G., Kimeridze, G. N., & Sigua, L. A. 2010, ApJ, 710, L126

Moderski, R., Sikora, M., Coppi, P. S., & Aharonian, F. 2005a, MNRAS, 364, 1488

—. 2005b, MNRAS, 363, 954

Mücke, A. & Protheroe, R. J. 2001, Astroparticle Physics, 15, 121

Mücke, A., Protheroe, R. J., Engel, R., Rachen, J. P., & Stanev, T. 2003, Astroparticle Physics, 18, 593

Nandra, K., George, I. M., Mushotzky, R. F., Turner, T. J., & Yaqoob, T. 1997, ApJ, 476, 70

Persson, S. E., Murphy, D. C., Krzeminski, W., Roth, M., & Rieke, M. J. 1998, AJ, 116, 2475

Pian, E., Vacanti, G., Tagliaferri, G., Ghisellini, G., Maraschi, L., Treves, A., Urry, M., Fiore, F., Giommi, P., Palazzi, E., Chiappetti, L., & Sambruna, R. M. 1998, ApJ, 492, L17+

Raiteri, C. M., Villata, M., Larionov, V. M., Pursimo, T., Ibrahimov, M. A., Nilsson, K., Aller, M. F., Kurtanidze, O. M., Foschini, L., Ohlert, J., Papadakis, I. E., Sumitomo, N., Volvach, A., Aller, H. D., Arkharov, A. A., Bach, U., Berdyugin, A., Böttcher, M., Buemi, C. S., Calcidese, P., Charlot, P., Delgado Sánchez, A. J., di Paola, A., Djupvik, A. A., Dolci, M., Efimova, N. V., Fan, J. H., Forné, E., Gomez, C. A.,

Gupta, A. C., Hagen-Thorn, V. A., Hooks, L., Hovatta, T., Ishii, Y., Kamada, M., Konstantinova, T., Kopatskaya, E., Kovalev, Y. A., Kovalev, Y. Y., Lähteenmäki, A., Lanteri, L., Le Campion, J.-F., Lee, C.-U., Leto, P., Lin, H.-C., Lindfors, E., Mingaliev, M. G., Mizoguchi, S., Nicastro, F., Nikolashvili, M. G., Nishiyama, S., Östman, L., Ovcharov, E., Pääkkönen, P., Pasanen, M., Pian, E., Rector, T., Ros, J. A., Sadakane, K., Selj, J. H., Semkov, E., Sharapov, D., Somero, A., Stanev, I., Strigachev, A., Takalo, L., Tanaka, K., Tavani, M., Torniainen, I., Tornikoski, M., Trigilio, C., Umana, G., Vercellone, S., Valcheva, A., Volvach, L., & Yamanaka, M. 2007, A&A, 473, 819

Ramos, E., Kafatos, M., Fruscione, A., Bruhweiler, F. C., McHardy, I. M., Hartman, R. C., Titarchuk, L. G., & von Montigny, C. 1997, ApJ, 482, 167

Remillard, R. A. & McClintock, J. E. 2006, ARA&A, 44, 49

Scargle, J. D. 1981, ApJS, 45, 1

Sikora, M., Begelman, M. C., & Rees, M. J. 1994, ApJ, 421, 153

Sikora, M. & Madejski, G. 2000, ApJ, 534, 109

Smith, D. M., Dawson, D. M., & Swank, J. H. 2007, ApJ, 669, 1138

Sun, W. & Malkan, M. A. 1989, ApJ, 346, 68

Tavecchio, F., Maraschi, L., Sambruna, R. M., & Urry, C. M. 2000, ApJ, 544, L23

Urry, C. M. & Mushotzky, R. F. 1982, ApJ, 253, 38

Urry, C. M. & Padovani, P. 1995, PASP, 107, 803

Vaughan, S., Edelson, R., Warwick, R. S., & Uttley, P. 2003, MNRAS, 345, 1271